

# Quantification of Reynolds-averaged-Navier-Stokes model form uncertainty in transitional boundary layer and airfoil flows

Minghan Chu,<sup>1, a)</sup> Xiaohua Wu,<sup>1, b)</sup> and David E. Rival<sup>2</sup>

<sup>1)</sup>*Mechanical and Aerospace Engineering, Royal Military College of Canada, Kingston, ON K7K 7B4, Canada.*

<sup>2)</sup>*Mechanical and Materials Engineering Department, Queen's University, Kingston, ON K7L 2V9, Canada.*

(\*Electronic mail: 17mc93@queensu.ca.)

(Dated: 19 July 2022)

It is well known that Boussinesq turbulent-viscosity hypothesis can introduce uncertainty in predictions for complex flow features such as separation, reattachment, and laminar-turbulent transition. This study adopts a recent physics-based uncertainty quantification (UQ) approach to address such model form uncertainty in Reynolds-averaged Navier-Stokes (RANS) simulations. Thus far, almost all UQ studies have focused on quantifying the model form uncertainty in turbulent flow scenarios. The focus of the study is to advance our understanding of the performance of the UQ approach on two different transitional flow scenarios: a flat plate and a SD7003 airfoil, to close this gap. For the T3A (flat-plate flow) flow, most of the model form uncertainty is concentrated in the laminar-turbulent transition region. For the SD7003 airfoil flow, the eigenvalue perturbations reveal a decrease as well as an increase in the length of the separation bubble. As a consequence, the uncertainty bounds successfully encompass the reattachment point. Likewise, the region of reverse flow that appear in the separation bubble is either suppressed or bolstered by the eigenvalue perturbations. In this context, the UQ methodology is applied to transition and show great results. This is the first successful RANS UQ study for transitional flows.

## I. INTRODUCTION

Transitional flow regime is very frequently encountered in turbomachines and especially in aircraft engines at relatively low Reynolds numbers. As a consequence, a significant part of the flow on the blade surfaces is under the laminar-turbulent transition process. The boundary development, losses, efficiency, and momentum transfer are greatly affected by the laminar-turbulent transition. Therefore, accurate prediction for the transition process is crucial for the design of efficient as well as reliable machines<sup>1</sup>.

Reynolds-averaged Navier-Stokes (RANS) simulations remain the most commonly used computational technique for analysis of turbulent flows. There has been considerable effort spent in the past two decades to develop RANS-based transition models for engineering applications to predict various kinds of transitional flows<sup>2-8</sup>. Each model has its strengths and weaknesses, and by far the correlation-based transition models by Langtry and Menter<sup>5,6</sup> have been widely used in engineering industries, in particular, aerospace industry. Most RANS models have adopted the Boussinesq turbulent viscosity hypothesis, i.e., anisotropy Reynolds stresses are proportional to the mean rate of strain, therefore also referred to as linear eddy viscosity models. It is well known that linear eddy viscosity models are limited due to the restrictions of the Boussinesq turbulent viscosity hypothesis, in particular, on yielding accurate predictions for complex flow fea-

tures such as separation-induced transition. Large eddy simulations (LES) or Direct numerical simulations (DNS) provide high-fidelity solution for such problems, but the calculations are often too expensive in computational time and cost, especially for high-Reynolds number flows. Therefore, uncertainty quantification (UQ) for the model form uncertainty is an valuable alternative route for improving the RANS predictive capability in engineering applications. More expensive LES or DNS would only be considered necessary if the model form uncertainty is too large.

The current study considers a physics-based approach that has been recently introduced by Emory *et al.*<sup>9</sup>, namely eigenspace perturbation method. This framework quantifies the model form uncertainty associated with the linear eddy viscosity model via sequential perturbations in the predicted amplitude (turbulence kinetic energy), shape (eigenvalues), and orientation (eigenvectors) of the anisotropy tensor. This perturbation method for RANS model uncertainty quantification has been applied to analyze and estimate the RANS uncertainty in flow through scramjets<sup>10</sup>, aircraft nozzle jets, turbomachinery, over stream-lined bodies<sup>11</sup>, supersonic axisymmetric submerged jet<sup>12</sup>, and canonical cases of turbulent flows over a backward-facing step<sup>13,14</sup>. This method has been used for robust design of Organic Rankine Cycle (ORC) turbine cascades<sup>15</sup>. In aerospace applications, this method has been used for design optimization under uncertainty<sup>16-19</sup>. In civil engineering applications, this method is being used to design urban canopies<sup>20</sup>, ensuring the ventilation of enclosed spaces, and used in the wind engineering practice for turbulent bluff body flows<sup>21</sup>. This perturbation method for RANS model uncertainty quantification has been used in conjunction with Machine Learning algorithms to provide precise estimates of RANS model uncertainty in the presence of data<sup>22-28</sup>. The method is also being used for the creation of probabilistic

<sup>a)</sup>Also at Mechanical and Materials Engineering Department, Queen's University, Kingston, ON K7L 2V9, Canada.

<sup>b)</sup><https://www.rmc-cmr.ca/en/mechanical-and-aerospace-engineering/xiaohua-wu>

aerodynamic databases, enabling the certification of virtual aircraft designs<sup>29,30</sup>.

In contrast to the data-driven methods, the current approach does not require high-fidelity data as input, hence more generally applicable. A key feature is that most of the application of this perturbation method for RANS model uncertainty have been on fully developed turbulent flows. However, in many aerospace applications flows undergoing transition are important and we require reliable UQ for the RANS predictions for such transitional flows, while few studies of the performance of this UQ methodology in the prediction for RANS transition modeling thus far have been performed. In addition, most studies focused on the performance of the eigenspace perturbation approach on mean velocity profile, skin and/or pressure coefficient, and did not consider the turbulence quantities. The essence for eigenspace perturbation method to perturb the shape of the Reynolds stress tensor is to move a linear-eddy-viscosity predicted Reynolds stress anisotropy state to a new location on a barycentric map<sup>31</sup>. The concept of Reynolds stress anisotropy can be better understood by analyzing the anisotropy trajectories presented on this map. However, very few studies have been performed to analyze anisotropy states for transitional flows.

The goal of this paper is therefore to advance the understanding of the performance of the eigenspace perturbation approach for quantifying the model form uncertainty in RANS simulations for two different transitional flow scenarios: flow over a flat plate (zero-pressure gradient) and flow over an SD7003 airfoil. Specifically, the objectives are (1) to quantify the model form uncertainty in three different linear eddy viscosity models (two turbulence models and one transition model) to scrutinize the differences between them; (2) to analyze the anisotropy states for the transitional boundary layer over a SD7003 airfoil based on a widely used RANS transition model and the in-house DNS data<sup>32</sup> using both the barycentric and Lumley's invariant maps<sup>33-35</sup>; (3) to explore the performance of the eigenspace perturbation approach on various flow-related QoIs: mean velocity, local wall shear stress and pressure, Reynolds shear stress, and turbulent production rate. The in-house DNS database of<sup>32</sup> for the SD7003 configuration is used to support our exploration.

## II. METHODOLOGY

### A. Governing equations

The flow was assumed to be two-dimensional and incompressible. The RANS formulation of the continuity and momentum equations is as follows:

$$\frac{\partial \langle U_i \rangle}{\partial x_i} = 0, \quad (1)$$

$$\frac{D \langle U_j \rangle}{Dt} = -\frac{1}{\rho} \frac{\partial \langle P \rangle}{\partial x_j} + \nu \frac{\partial^2 \langle U_j \rangle}{\partial x_i \partial x_i} - \frac{\partial \langle u_i u_j \rangle}{\partial x_i} \quad (2)$$

where  $\langle \rangle$  represents time-averaging.  $\rho$  is the density,  $\langle P \rangle$  is the time-averaged pressure, and  $\mathbf{v}$  is the kinematic viscosity. The  $\langle U_i \rangle$  are the time-averaged velocity components. Reynolds stress terms in Eqs. 1 - 2, i.e.,  $\langle u_i u_j \rangle$ , are unknowns that need to be approximated using a RANS model. In this study, two-equation linear eddy viscosity models are used, which are based on the Boussinesq turbulent viscosity hypothesis as follows:

$$\langle u_i u_j \rangle = \frac{2}{3} k \delta_{ij} - 2\nu_t \langle S_{ij} \rangle, \quad (3)$$

where  $k$  is the turbulence kinetic energy,  $\delta_{ij}$  is the Kronecker delta,  $\nu_t$  is the turbulent viscosity, and  $\langle S_{ij} \rangle$  is the rate of mean strain tensor. In Eq. 3, the deviatoric anisotropic part is

$$\begin{aligned} a_{ij} &\equiv \langle u_i u_j \rangle - \frac{2}{3} k \delta_{ij} \\ &= -\nu_t \left( \frac{\partial \langle U_i \rangle}{\partial x_j} + \frac{\partial \langle U_j \rangle}{\partial x_i} \right) \\ &= -2\nu_t \langle S_{ij} \rangle. \end{aligned} \quad (4)$$

The normalized anisotropy tensor (used extensively) is defined by

$$b_{ij} = \frac{a_{ij}}{2k} = \frac{\langle u_i u_j \rangle}{2k} - \frac{\delta_{ij}}{3} = -\frac{\nu_t}{k} \langle S_{ij} \rangle. \quad (5)$$

In the results presented hereafter for the flat plate, three different linear eddy viscosity models were considered: the shear-stress transport (SST)  $k - \omega$ <sup>36-39</sup>, the modified version of SST  $k - \omega$  for transitional flow simulations by Langtry and Menter (SST  $k - \omega$  LM)<sup>3,5,40</sup>, and the  $k - \varepsilon$  model<sup>41,42</sup>. By considering three different models, we intend to contrast the uncertainty bounds generated by the transition model (SST  $k - \omega$  LM) with the two turbulence models (SST  $k - \omega$  and  $k - \varepsilon$ ). Results corresponding to these linear eddy viscosity models bereft of any perturbations are referred to as ‘‘baseline’’ solutions.

### B. Eigenspace perturbation method

The Reynolds stress tensor  $\langle u_i u_j \rangle$  is symmetric positive semi-definite<sup>34</sup>, thus it can be eigen-decomposed as follows:

$$\langle u_i u_j \rangle = 2k \left( \frac{\delta_{ij}}{3} + v_{in} \hat{b}_{nl} v_{jl} \right), \quad (6)$$

in which  $k \equiv u_i u_i / 2$ ,  $\mathbf{v}$  represents the matrix of orthonormal eigenvectors,  $\hat{\mathbf{b}}$  represents the diagonal matrix of eigenvalues ( $\lambda_i$ ), which are arranged in a non-increasing order such that  $\lambda_1 \geq \lambda_2 \geq \lambda_3$ . The amplitude, the shape and the orientation of  $\langle u_i u_j \rangle$  are explicitly represented by  $k$ ,  $\lambda_i$ , and  $v_{ij}$ , respectively. Equations 5 and 6 lead to

$$b_{ij} = -\frac{v_t}{k} \langle S_{ij} \rangle = v_{in} \hat{b}_{nl} v_{jl}. \quad (7)$$

Equation 7 indicates that the Boussinesq turbulent viscosity hypothesis requires that the shape and orientation of  $\langle u_i u_j \rangle$  to be determined by  $(v_t/k) \langle S_{ij} \rangle$ . This assumption implies the  $a_{ij}$  tensor is aligned with the  $\langle S_{ij} \rangle$  tensor, which is not true in most circumstances in practice, in particular, complex flows, e.g., strongly swirling flows, flow with significant streamline curvature, and flow with separation and reattachment, and thus a source of the model form uncertainty.

The eigenspace perturbation method was first proposed in<sup>43,44</sup>. To model errors introduced in the model form uncertainty, perturbation is injected into the eigen-decomposed Reynolds stress defined in Eq. 6. The perturbed Reynolds stress are defined as

$$\langle u_i u_j \rangle^* = 2k^* \left( \frac{1}{3} \delta_{ij} + v_{in}^* \hat{b}_{nl}^* v_{jl}^* \right), \quad (8)$$

where  $k^* = k + \Delta k$  is the perturbed turbulence kinetic energy,  $\hat{b}_{kl}^*$  is the diagonal matrix of perturbed eigenvalues, and  $v_{ij}^*$  is the perturbed eigenvector matrix. Perturbing  $k$  is an important component of the eigenspace perturbation framework. In reality, the coefficient of turbulent viscosity in the Boussinesq turbulent viscosity hypothesis varies between different turbulent flow cases and even between different regions in the same turbulent flow<sup>45</sup>; however, the Boussinesq turbulent viscosity hypothesis espouses a universal constant coefficient, which fails to capture the true physics of turbulent flow. According to Mishra and Iaccarino<sup>45</sup>, perturbations to turbulence kinetic energy spatially vary the coefficient of turbulent viscosity, and in a sense change the original Boussinesq turbulent viscosity hypothesis to anisotropy viscosity hypothesis. Thus, turbulence kinetic energy perturbation is important to describe the real behavior of turbulent flow. While few studies addressing the perturbations to turbulence kinetic energy have been conducted, it becomes a valuable future research direction. Eigenvector perturbations rotate the eigenvectors of the anisotropy Reynolds stress tensor with respect to the principal axes of the mean rate of strain. Recall that the eigenvectors of the anisotropy Reynolds stress tensor are forced to align along the principal axes of the mean rate of strain due to the limitations of the Boussinesq turbulent viscosity hypothesis<sup>34</sup>. This again violates the true physics of turbulent flow. Consequently, eigenvector perturbations extend the Boussinesq turbulent viscosity hypothesis to anisotropy turbulent viscosity hypothesis. Unlike eigenvalue perturbations, which are strictly constrained by realizability. Eigenvector perturbations are more difficult to be physically constrained in a local sense. In the current study, eigenvector perturbations are omitted for brevity. For these reasons, the present study restricts the contribution to eigenvalue perturbations  $\hat{b}_{ij}^*$ . Due to the realizability constraint of the semi-definiteness of  $\langle u_i u_j \rangle$ , there are three extreme states of componentiality of  $\langle u_i u_j \rangle$ : one component limiting state (1C), which has one non-zero principal

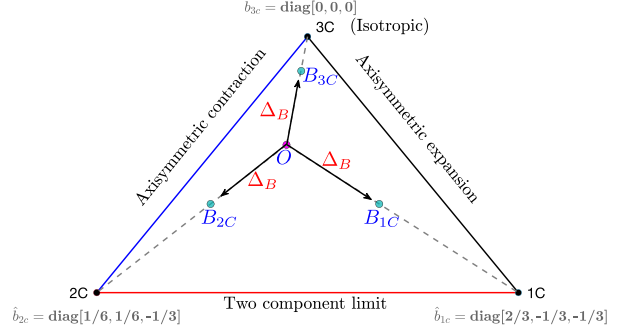


FIG. 1. Barycentric map.

fluctuation, i.e.,  $\hat{b}_{1c} = \text{diag}[2/3, -1/3, -1/3]$ ; two component limiting state (2C), which has two non-zero principal fluctuations of the same intensity, i.e.,  $\hat{b}_{2c} = \text{diag}[1/6, 1/6, -1/3]$ ; and three component (isotropic) limiting state (3C), which has three non-zero principal fluctuations of the same intensity, i.e.,  $\hat{b}_{3c} = \text{diag}[0, 0, 0]$ .

For eigenvalue perturbations, Pecnik and Iaccarino<sup>43</sup> proposed a perturbation approach, which enforces the realizability constraints on  $\langle u_i u_j \rangle$  via the barycentric map<sup>31</sup>, as shown in Fig. 1, because the map contains all realizable states of  $\langle u_i u_j \rangle$ . In addition, the  $\hat{b}_{1c}$ ,  $\hat{b}_{2c}$ , and  $\hat{b}_{3c}$  limiting states correspond to the three vertices of the barycentric map. Given an arbitrary point  $\mathbf{x}$  within the barycentric map, any realizable  $\langle u_i u_j \rangle$  can be determined by a convex combination of the three vertices  $\mathbf{x}_{ic}$  (limiting states) and  $\lambda_i$  as follows:

$$\mathbf{x} = \mathbf{x}_{1c} (\lambda_1 - \lambda_2) + \mathbf{x}_{2c} (2\lambda_2 - 2\lambda_3) + \mathbf{x}_{3c} (3\lambda_3 + 1). \quad (9)$$

In order to define the perturbed eigenvalues  $\hat{b}_{ij}^*$ , first determine the location for the Reynolds stress computed by a linear eddy viscosity model and subsequently inject uncertainty by shifting it to a new location on the barycentric map. In Fig. 1, perturbations toward 1c, 2c, and 3c vertices of the barycentric map shift point  $O$  to  $B_{1c/2c/3c}$ , respectively, which can be written as

$$\mathbf{x}_{B(1c/2c/3c)}^* = \mathbf{x}_O + \Delta_B (\mathbf{x}_{1c/2c/3c} - \mathbf{x}_{B(1c/2c/3c)}), \quad (10)$$

where  $\Delta_B$  is the magnitude of perturbation toward the three vertices. Once the new location is determined, a new set of eigenvalues  $\lambda_i$  can be computed from Eq. 9 and to reconstruct  $b_{ij}$ , which eventually yields  $\langle u_i u_j \rangle^*$ .

### C. Eigenspace perturbation framework in OpenFOAM

This study contributes the eigenspace perturbation framework<sup>9</sup> to both the “simpleFOAM” (steady) and “pimpleFOAM” (transient) solvers in the open source OpenFOAM

software<sup>46</sup>. Most previous studies on the model form uncertainty have used the open source OpenFOAM software<sup>46</sup> compounded with the Matlab software to decompose and recombine the Reynolds stress tensor, e.g., see<sup>14,47</sup>. In this study, a new class of the eigenspace perturbation framework written in the 100% OpenFOAM-version of C++ was created and injected in the top level classes in OpenFOAM, which greatly reduces the number of user-defined inputs. This allows the users without much knowledge of the fluid mechanics to use the eigenspace perturbation method in OpenFOAM.

The magnitude of perturbation  $\Delta_B$  and which eigenvalue perturbation (1c,2c,3c) to be performed are specified by the user in the input files located under the “Constant” directory in OpenFOAM, and C++ code with customized OpenFOAM data type is added to the existing code base that conducts the perturbations during the execution of simulations, as shown in Fig. 2. At each control volume (CV), the baseline Reynolds stress tensor is calculated and decomposed into its eigenvalue and eigenvector matrices, which are perturbed using the eigenspace perturbation method as prescribed earlier. The perturbed eigenvalue and eigenvector matrices are then recomposed into a perturbed Reynolds stress tensor for each CV. These perturbed Reynolds stress tensors are then used to compute the perturbed velocity field and the perturbed turbulent production to advance each node to the next (pseudo) time step. At convergence, the Reynolds stress also converges to its perturbed state.

### III. FLOW DESCRIPTION AND NUMERICAL METHOD

In this study, the eigenspace perturbation method was used to test several RANS models in the prediction for the laminar-turbulent transition process that occurs for incompressible transitional flow over two different geometries: ERCOFTAC T3A<sup>48</sup> and SD7003 airfoil. Details of these two flow configurations are presented below.

#### A. T3A

One flow being considered is the ERCOFTAC T3A case over a flat plate (zero pressure gradient), as shown in Fig. 3. The solution domain is two-dimensional and uses a Cartesian coordinate system. The computational domain is 3.0 m (L) long and 1.0 m (H) high in the streamwise (x) and wall-normal (y) direction, respectively. The simulation results based on the nonuniform grids of 340 and 60 control volumes in the streamwise and wall-normal direction, respectively. The first grid node in the wall-normal direction was placed at a value of  $y^+ < 1$  over the entire plate, and the effect of refining the mesh in the y-direction on the prediction for the skin friction coefficient was much less than 1%. The fluid was assumed to be air, with freestream turbulence intensity of  $Tu = \sqrt{2k/3}/U_\infty = 3.3\%$ , where  $U_\infty$  represents the freestream velocity, and kinematic viscosity of  $\nu = 1.5 \times 10^{-5} \text{ m}^2/\text{s}$ . For

the smooth flat plate, a no-slip boundary condition was assumed. At the inlet of the domain, the freestream velocity was set equal to  $U_\infty = 5.4 \text{ m/s}$ . A slip boundary condition was specified for  $\langle U_i \rangle$  ( $U$  for  $x$  direction and  $V$  for  $y$  direction) at the top of the domain, and a zero-gradient for  $k$ ,  $\omega$  and pressure at the outlet and the top of the domain. Upstream of the leading edge has a space that allows the flow to develop before encountering the leading edge, as shown in Fig. 3. The governing Eqs. 1 - 2 together with the transport equation for the SST  $k - \omega$  LM model were solved using the open source software OpenFOAM<sup>49</sup>. The transport equations were discretized using finite volume method. The scheme is second order upwind for spatial discretization of flow quantities, and Gauss linear scheme was used to evaluate the gradients. The pressure-velocity coupling adopted the SIMPLEC (Semi-Implicit Method for Pressure Linked Equations-Consistent)<sup>50</sup> algorithm. The solution fields were iterated until convergence: the residuals leveled out and no discernible change in the solution was observed.

#### B. SD7003

Second flow being considered is around an SD7003 airfoil, as shown in Fig. 4. At the low Reynolds number based on chord length of  $Re_c = 60000$ , a laminar separation bubble (LSB) is formed on the suction side of the airfoil. Note that the bubble moves upstream as the angle of attack (AoA) increases<sup>51</sup>. In this study, an  $8^\circ$  AoA (nearing stall) was considered. Figure 4 schematically shows that the solution domain is a two-dimensional C-topology grid of  $389$  (streamwise)  $\times$   $280$  (wall-normal)  $\times$   $1$  (spanwise) control volumes, which is comparable to the number of control volumes ( $768 \times 176$ ) used in the numerical study of<sup>51</sup>. The magnified view of the two-dimensional SD7003 airfoil labels the camber, suction side and pressure side, as shown in Fig. 4. The first grid node to the wall was placed at  $y^+ \approx 1.0$  in the turbulent region, in which more than 20 CVs were placed. The governing Eqs. 1 - 2 together with the transport equation for the chosen RANS model were solved using the open source software OpenFOAM<sup>49</sup>. The transport equations were discretized using finite volume method. The scheme was second order upwind for spatial discretization of flow quantities, and Gauss linear scheme was used to evaluate the gradients. To deal with unsteady flows, PIMPLE algorithm was adopted for pressure-velocity coupling, which is a combination of PISO (Pressure Implicit with Splitting of Operator)<sup>52</sup> and SIMPLEC<sup>50</sup>. It should be noted that PIMPLE algorithm can deal with large time steps where the maximum Courant (C) number may consistently be above 1. In this study, the maximum value of C was set consistently equal to 0.6, and the time step was varied automatically in OpenFOAM to achieve the set maximum. In addition, both residuals and distributions of lift and drag coefficients that vary with respect to time ( $T$ ) were used to track convergence status. The solution fields were iterated until convergence, which required residuals of turbulence kinetic energy and momentum to drop more than four orders of magnitude, and both lift and drag coefficients leveled out

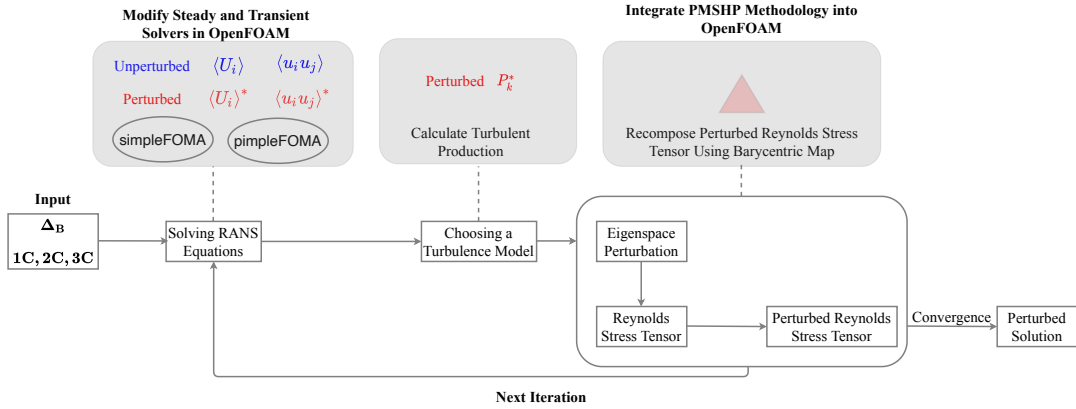


FIG. 2. Flow chart showing the implementation of eigenspace perturbation framework within OpenFOAM.

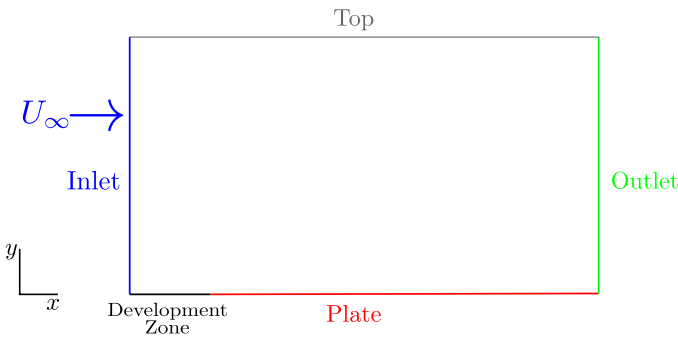


FIG. 3. T3A computational domain. — blue — inflow ( $U_\infty$ ), — green — outflow, — red —, no-slip wall, — grey —, Top, — black —, and flow-development zone.

TABLE I. Number of computational cells.

	Coarse	Medium	Fine
Number of cells	93k	110k	148k

with respect to time. This happened at  $T \approx 0.3$ , which corresponds to a normalized time  $T^* = TU_\infty/c = 6.75$ , and similar behavior has been observed by Catalano and Tognaccini<sup>51</sup> in their numerical study for a low-Reynolds number flow over a SD7003 airfoil at  $\text{AoA} = 10^\circ$ . Sampling began at  $T = 0.6$  (double the time of convergence) and ended at  $T = 1.4$ , which required approximately 35000 iterations for all simulations.

The fluid was assumed to be air, with freestream turbulence intensity of  $Tu = 0.03\%$  and kinematic viscosity of  $\nu = 1.5 \times 10^{-5} \text{ m}^2/\text{s}$ . Ideally, the value of  $Tu$  should be close to zero. From Fig. 4 at the inlet of the domain, the freestream velocity was set equal to  $4.5 \text{ m/s}$ , which corresponds to  $\text{Re}_c = 60000$ . The chord length was set equal to  $c = 0.2 \text{ m}$ . At the outlet, a zero-gradient boundary condition was implemented for  $\langle U_i \rangle$  ( $\langle U \rangle$  for  $x$  direction,  $\langle V \rangle$  for  $y$  direction),  $k$ ,  $\omega$  and pressure. At the wall, a no-slip boundary condition was used.

A grid convergence study of the SST  $k - \omega$  LM simula-

tions has been performed to test the influence of the grid resolution on the results. Simulations with three different levels of mesh resolution are summarized in Table I. The refinement was concentrated in the vicinity of the wall where high spatial gradients are present. Negligible difference in the predictions for the skin friction coefficient  $C_f = \tau_w/0.5\rho U_\infty^2$ , where  $\tau_w$  is the wall shear stress, and the pressure coefficient  $C_p = (p - p_\infty)/0.5\rho U_\infty^2$ , where  $p$  is the static pressure and  $p_\infty$  is the static pressure in the freestream, were observed among the coarse, medium, and fine meshes. Moreover, only a slight difference in the results based on the coarse mesh and the other two meshes (medium and fine) was observed, i.e., the results based on the medium and fine mesh almost collapsing onto a single curve. In addition, the mean flow ( $\langle U \rangle/U_\infty$ ) and turbulence quantities ( $-\langle u_1 u_2 \rangle/U_\infty^2$ ) exhibit a slight difference between the coarse mesh and the other two levels (medium and fine), for which the difference was at almost 1%. Therefore, a mesh with  $768 \times 176$  (medium) has been considered sufficiently accurate and used for the simulations hereafter.

## IV. RESULTS AND DISCUSSION

### A. Transitional flow over a smooth flat plate with zero pressure gradient

In this section, the eigenspace perturbation framework is tested on three different RANS models: SST  $k - \omega$  LM<sup>3,5,40</sup>, SST  $k - \omega$ <sup>36-39</sup>, and  $k - \epsilon$ <sup>41,42</sup>. The baseline predictions are first presented, followed by eigenvalue perturbations to the anisotropy tensor.

#### 1. Skin friction coefficient

Perhaps the local wall shear stress is the most important parameter for a boundary layer, which in dimensionless form becomes  $C_f$ . In Fig. 5, the baseline SST  $k - \omega$  LM prediction

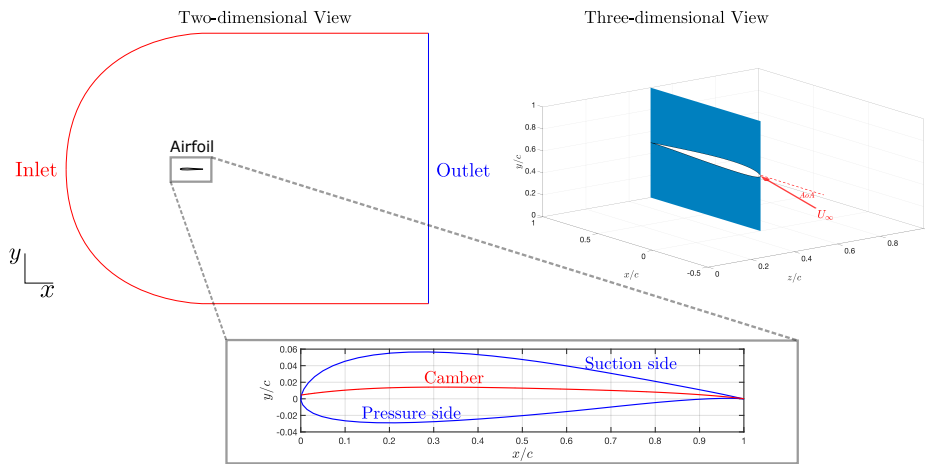


FIG. 4. SD7003 computational domain and boundary conditions: — far field, — outflow, —, and no-slip walls. Depiction of the suction side, camber, and pressure side of the SD7003 airfoil is displayed in the magnified plot. A three-dimensional version of the computational domain is provided with freestream ( $U_\infty$ ) encountering the leading edge at  $8^\circ$  AoA.

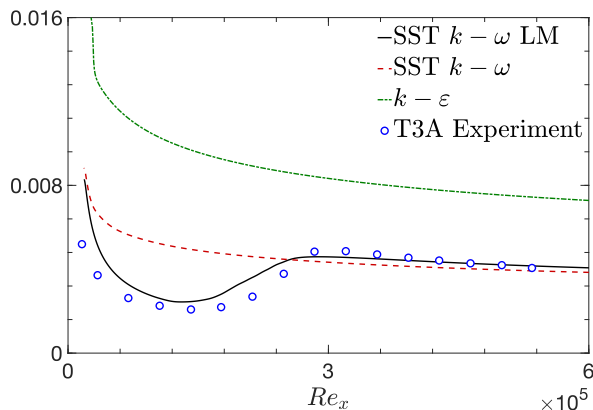


FIG. 5. Prediction for skin friction coefficient distribution over a flat plate.

for  $C_f$  is plotted with respect to the Reynolds number based on local distance from the leading edge  $Re_x$ , along with other two popular RANS turbulence models SST<sup>36–39</sup> and  $k-\epsilon$ <sup>41,42</sup> for reference. No slip boundary condition was assumed at the solid wall surface for all three RANS models, which are integrated down to the wall. The ERCOFTAC experimental data of<sup>48</sup> is included for comparison. Figure 5 clearly shows a “trough” in the experimental data, which marks the laminar-turbulent transition process. The predicted  $C_f$  profile of SST  $k-\omega$  LM<sup>3,5,40</sup> lies somewhat above the experimental data of<sup>48</sup> in the transitional region, while lies slightly below the experimental data as the flow moves further downstream in the fully turbulent region, but overall shows good agreement with the dataset across the entire flat plate. On the other hand, the predicted  $C_f$  profile of SST  $k-\omega$ <sup>36–39</sup> shows good agreement with the ERCOFTAC data of<sup>48</sup> in the fully turbulent region downstream of the trough, but fails to capture the behavior of laminar-turbulent transition. However, the  $k-\epsilon$  model<sup>41,42</sup>

significantly over-predicts the value of  $C_f$  across the entire flat plate compared to the ERCOFTAC data of<sup>48</sup>, as shown in Fig. 5.

## 2. Mean flow field

The baseline predictions for contours of the mean velocity normalized with the free stream velocity,  $\langle U \rangle / U_\infty$  in an  $xy$  plane are presented in Fig. 6. Figure 6 magnifies the region close to the leading edge for  $0 < x/L < 0.2$ , which corresponds to  $0 < Re_x < 2.16 \times 10^5$  (at the trough). In this region, the SST  $k-\omega$  LM transition model<sup>3,5,40</sup> shows a “bump” next to the wall, giving a lower magnitude of  $\langle U \rangle / U_\infty$  compared to the SST turbulence model<sup>36–39</sup>, although a lower value of  $C_f$  is found at the trough shown in Fig. 5. As the bump alters the effective shape of the geometry, we conjecture that an additional “form-induced drag” might be generated, which might explain the reduction in the magnitude of  $\langle U \rangle / U_\infty$ . However, it is clear that no discernible bump around the leading edge is observed for both the SST<sup>36–39</sup> and  $k-\epsilon$  turbulence models<sup>41,42</sup>, which indicates that both models fail to capture the laminar-turbulent transition process. This confirms the behavior shown in Fig. 5. In addition, the  $k-\epsilon$  turbulence model overall gives a much smaller value of  $\langle U \rangle / U_\infty$  than the other two models, which confirms the significantly increased value of  $C_f$  along the entire flat plate, as shown in Fig. 5.

The baseline predictions for the  $\langle U \rangle / U_\infty$  profiles at different locations using the three different models are plotted in Fig. 7. From Fig. 7, it is clear that the SST  $k-\omega$  LM transition model gives the velocity profiles at  $x = 0.2, 0.4$  and  $0.6$  ( $x/c = 0.067, 0.13$  and  $0.2$ ) lagging behind the ones produced by the SST  $k-\omega$  turbulence model. This confirms the behavior observed in Fig. 6, indicating that the effect of wall shear stress of the SST  $k-\omega$  LM model is enhanced in the vicinity of the wall, i.e., the greatest reduction in momentum by the SST  $k-\omega$  LM model. The decrease in momentum

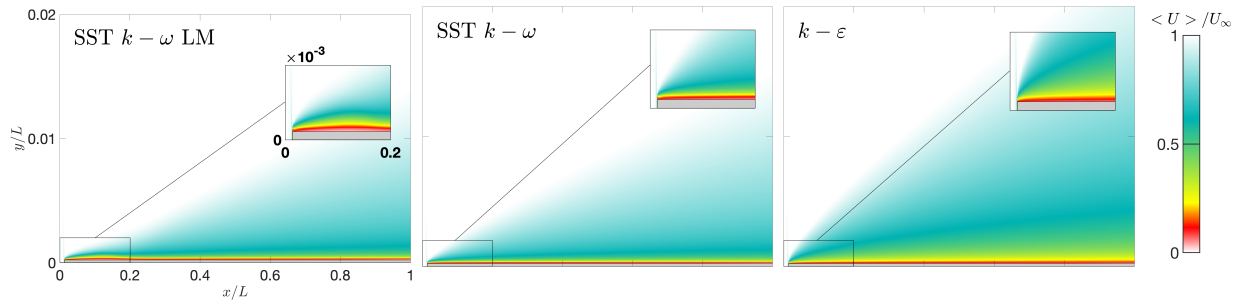


FIG. 6. Contours of streamwise mean velocity over a flat plate. The region close to the leading edge is enlarged for  $0 < x/c < 0.2$ .

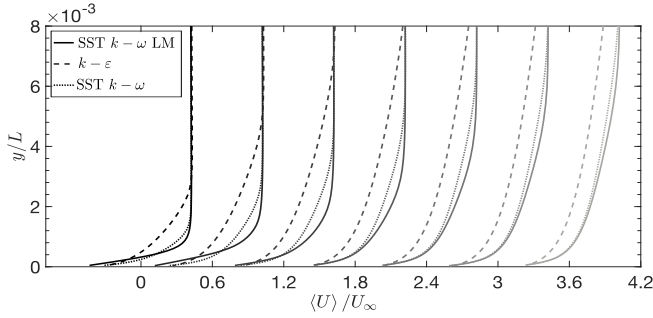


FIG. 7. Profile of normalized mean velocity using three different models. From left to right are profiles at  $x = 0.2, 0.4, 0.6, 0.8, 1.0, 1.2, 1.4$  ( $x/c = 0.067, 0.13, 0.20, 0.27, 0.33, 0.40, \text{ and } 0.47$ ).

propagates higher into the boundary layer as the flow proceeds downstream of the leading edge. In the outer region, all of the velocity profiles recover to the freestream value. In addition, the velocity profile produced by the SST  $k - \omega$  LM model begins to lead ahead to the velocity profiles produced by the SST  $k - \omega$  and  $k - \varepsilon$  models. This reflects that the effect of wall shear stress weakens more quickly for the SST  $k - \omega$  LM model than the SST  $k - \omega$  and  $k - \varepsilon$  models. It is interesting to note that the difference between the profiles produced by the SST  $k - \omega$  and SST  $k - \omega$  LM models becomes smaller as the flow moves further downstream in the turbulent boundary layer. This confirms the behavior shown in Fig. 5, i.e., difference in  $C_f$  is rather small downstream of the trough. This is due to the fact that in the turbulent region only are the SST  $k - \omega$  model formulations triggered in the SST  $k - \omega$  LM model<sup>5</sup>. On the other hand, the velocity profile produced by the  $k - \varepsilon$  model overall lags behind the other two models, indicating the effect of wall shear is rather significant throughout the entire boundary layer, which confirms the behavior shown in Fig. 5.

### 3. Wall shear stress: uniform $\Delta_B$

The eigenspace perturbation framework is tested on three different RANS models: SST  $k - \omega$  LM<sup>3,5,40</sup>, SST  $k - \omega$ <sup>36-39</sup>, and  $k - \varepsilon$ <sup>41,42</sup>. Figure 8 shows the predictions for  $C_f$  as a

function of  $Re_x$ . Also included is the ERCOFTAC experimental data of<sup>48</sup> for comparison. In Fig. 8, an “enveloping behavior” with respect to the baseline prediction is observed, and this behavior has been observed by other researchers as well, e.g., see<sup>9,11-13</sup>. In Fig. 8, the simulation’s response to different values of  $\Delta_B$  varies with which model is being used. For SST  $k - \omega$  LM, there are two important observations: first, the uncertainty bound is almost concentrated in the transitional region where the  $C_f$  profile begins to recover toward the fully turbulent profile. Second, in the recovery region the 1c and 2c perturbations under-predict the baseline prediction ( $\downarrow C_f$ ), while the 3c perturbation does the opposite ( $\uparrow C_f$ ); however, in the fully turbulent region it is the complete opposite of the behavior observed in the recovery region. The 1c perturbation shows a tendency to encompass the reference data, which reflects that the increased streamwise stresses contribute to a reduced  $C_f$  value in the recovery region. The 3c perturbation does the opposite, reflecting isotropic stresses tend to increase the value of  $C_f$  in the recovery region. It is clear that the eigenvalue perturbations are not sufficient to encompass all the reference data. This might be due to the exclusion of the amplitude and eigenvector perturbation of the Reynolds stress tensor, and the parametric uncertainty introduced in the model coefficients. In addition, the response to  $\Delta_B$  appears to be linear, i.e., the  $\Delta_B = 1$  envelope is twice the envelope of  $\Delta_B = 0.50$ , which also is twice the envelope of  $\Delta_B = 0.25$ . With increasing  $\Delta_B$ , the 1c and 2c perturbations from SST  $k - \omega$  LM tend to encompass the experimental data, while the 3c perturbation deviates from the experimental data. For SST  $k - \omega$ , the response to  $\Delta_B$  is relatively small, and the uncertainty bound tends to increase linearly with  $\Delta_B$ , with 1c and 2c profiles sitting above the baseline prediction while the 3c profile sitting slightly below the baseline prediction. In addition, more experimental data in the turbulent region are encompassed when the value of  $\Delta_B$  is increased. On the other hand, the  $k - \varepsilon$  model’s response to  $\Delta_B$  is larger than that for SST  $k - \omega$ , and again appears to be linear with  $\Delta_B$ ; however, it is clear that the  $k - \varepsilon$  model overall gives much larger predicted value of  $C_f$  than the experimental data; consequently, no experimental data are encompassed by the uncertainty bound generated from the  $k - \varepsilon$  model. It should be noted that thus far most UQ studies have focused on turbulent flow simulations, from which the 1c and 2c perturbations

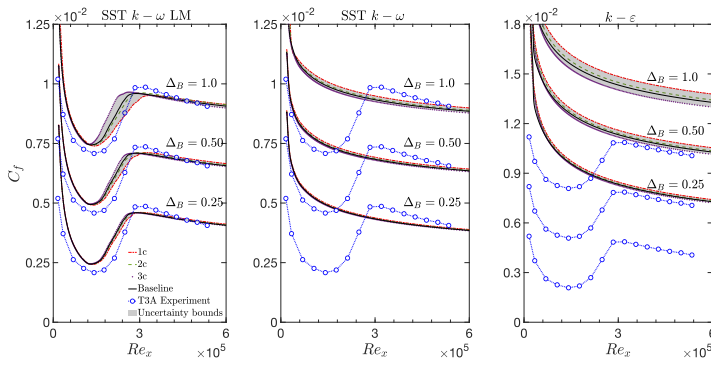


FIG. 8. Distribution of skin friction coefficient over a flat plate. Uncertainty bounds (gray envelope) with different magnitudes of  $\Delta_B$ . The baseline prediction (solid line) is provided for reference. Each profile is shifted vertically by a same distance for each model.

always increase the value of  $C_f$ , while the opposite is true for the  $3c$  perturbation, e.g., see<sup>12,47,53</sup>, which is consistent with the behavior observed with the SST  $k - \omega$  and  $k - \epsilon$  turbulence models, as well as the behavior observed in the fully turbulent region with the SST  $k - \omega$  LM transition model.

#### 4. Turbulence intensity: $1c$ , $2c$ , and $3c$ ( $\Delta_B = 1$ )

Figure 9 shows decaying of  $Tu$  in freestream as a function of  $Re_x$ . Also included is the ERCOFTAC experimental data of<sup>48</sup>. Figure 9 clearly shows that the baseline predictions for the  $Tu$  profiles using SST  $k - \omega$  LM<sup>3,5,40</sup>, SST  $k - \omega$ <sup>36-39</sup>, and  $k - \epsilon$ <sup>41,42</sup> are almost indistinguishable from each other, indicating a type of similarity. This indicates that the effect of these different linear eddy viscosity models is restricted to the near-wall region, and the flow becomes insensitive to which model is being used in the freestream region far from the wall. In addition, these three models show good agreement with the experimental data, and show little response to the eigenvalue perturbations ( $1c$ ,  $2c$ ,  $3c$ ), i.e., negligible uncertainty bounds. This indicates a low level of model form uncertainty in the baseline predictions for  $Tu$  decaying in freestream.

#### 5. Turbulence kinetic energy: $1c$ , $2c$ , and $3c$ ( $\Delta_B = 1$ )

Figure 10 shows contours of the turbulence kinetic energy normalized with the freestream velocity squared,  $k/U_\infty^2$  from the baseline, eigenvalue perturbations ( $1c$ ,  $2c$ , and  $3c$ ) in an  $xy$  plane. It is clear that a “bump” again appears close to the leading edge, which is similar to the behavior for SST  $k - \omega$  LM shown in Fig. 6. The laminar-turbulent transition happens in the bump, where it tends to induce a lower value of  $k/U_\infty^2$ . Compared to the baseline prediction, an overall reduction in the magnitude of  $k/U_\infty^2$  is observed for the  $1c$  and  $2c$  perturbations, while the  $3c$  perturbation does the opposite. In addition, the  $1c$  perturbation increases the bump length more than the  $2c$  perturbation does (bolstering the laminar-

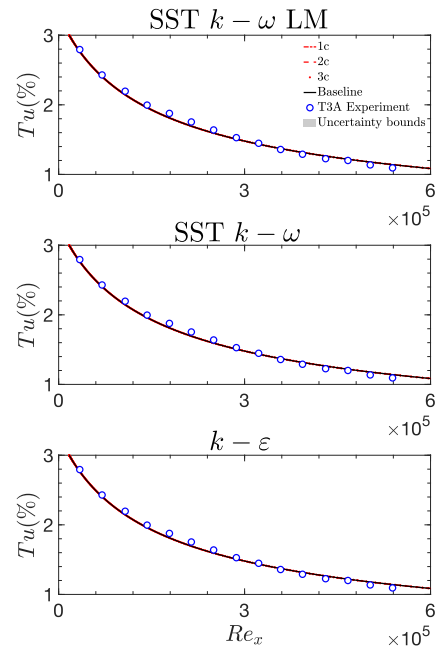


FIG. 9. Freestream turbulence intensity decay for T3A. Uncertainty bounds (gray region) for  $1c$ ,  $2c$ , and  $3c$  perturbations (uniform  $\Delta_B = 1$ ) are displayed. The baseline prediction (solid line) is provided for reference.

turbulent transition). On the other hand, the  $3c$  perturbation shortens the bump length (suppressing the laminar-turbulent transition). We note that the  $1c$  and  $2c$  perturbations overall reduced the velocity magnitude during the laminar-turbulent transition (in the bump), while the  $3c$  perturbation increased the velocity magnitude (perturbed velocity contours are omitted for brevity). Given this, it is interesting to conclude that the size of the transitional region is in a sense inversely related to the mean velocity magnitude under eigenvalue perturbations, e.g.,  $\uparrow$  transitional region and  $\downarrow \langle U \rangle$ . This suggests that lower local freestream velocity yields less shear stress, which in turn slows down the progression of transition.

## B. Transitional flow over a SD7003 airfoil

In this section, the eigenspace perturbation framework is used to introduce uncertainty in the SST  $k - \omega$  LM model<sup>3,5,40</sup>, and the eigenvalue perturbations with  $\Delta_B = 1$  ( $1c$ ,  $2c$ ,  $3c$ ) are conducted. To begin with, two different values of  $Tu = 0.03\%$  (very low freestream turbulence intensity) and  $Tu = 0.5\%$  (low freestream turbulence intensity) are used to test the sensitivity to the framework. Note that special focus is given to the eigenvalue perturbations for  $Tu = 0.03\%$ .

### 1. Crucial transition parameters

Figures 11 (a) and (b) show the baseline predictions for the distributions of  $C_f$  and  $C_p$ . Also included are the in-house



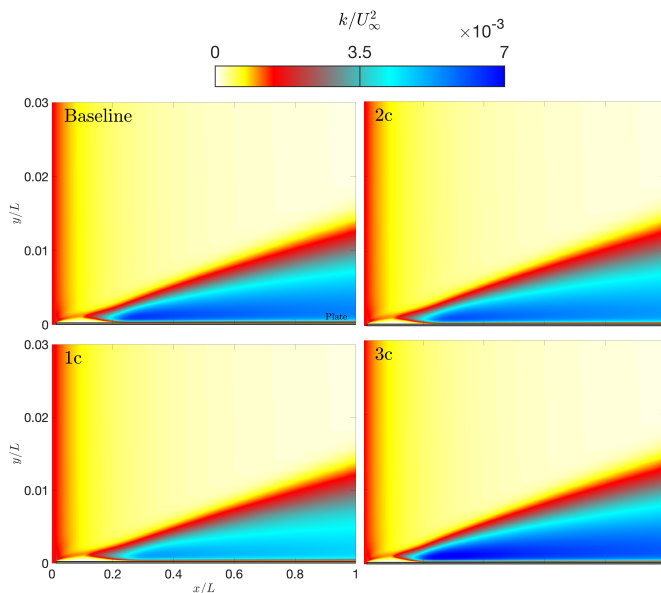


FIG. 10. Contours of turbulence kinetic energy for 1c, 2c, and 3c perturbations using the SST  $k - \omega$  LM model over a flat plate. The baseline prediction is provided for reference.

DNS<sup>32</sup> and Implicit LES (ILES)/LES data of<sup>54</sup> and<sup>55</sup> for comparison. Figure 11 (c) schematically defines a transitional region and a turbulent region on the upper surface of the airfoil. Figure 11 (a) shows a region of nearly constant pressure or a “flat spot”<sup>56</sup> that marks the presence of the LSB<sup>57,58</sup>. The separation, transition and reattachment points are the critical transition parameters that can be approximated with either  $C_p$  or  $C_f$  plot. According to the technique described by Boutilier and Yarusevych<sup>59</sup>, Fig. 11 (a) shows three “kinks” as representatives of the separation, transition and reattachment points, denoted  $X_S/c$ ,  $X_T/c$  and  $X_R/c$ , respectively. From Fig. 11 (b), finding the zeros of the skin friction coefficient is a different technique that can be used to approximate the  $X_S/c$ ,  $X_T/c$  and  $X_R/c$  points as well<sup>60</sup>. Based on the reference data, both techniques showed good agreement with each other, and a summary of these transition parameters is presented in Table II. Overall, the baseline predictions for  $Tu = 0.03\%$  show better agreement with the reference data than  $Tu = 0.5\%$ . This is due to the fact that the value of  $Tu = 0.03\%$  more closely matches that for the reference data, i.e.,  $Tu \approx 0\%$ . In this study, the LSB is treated to be composed of a “fore” (from  $X_S/c$  to  $X_T/c$ ) and an “aft” (from  $X_T/c$  to  $X_R/c$ ) portion for the sake of investigation simplicity, followed by a fully turbulent region, as shown in Fig. 11 (c).

In Fig. 11 (a), the predictions for  $C_p$  with  $Tu = 0.03\%$  and  $Tu = 0.5\%$  show good agreement with the ILES data of<sup>54</sup>, as well as with the in-house DNS<sup>32</sup> and LES data of<sup>55</sup> at the flat spot (in the fore portion of the LSB), respectively, followed by a discrepancy in the pressure recovery region in the aft portion of the LSB. After the  $X_R/c$  point, the  $C_p$  profile for  $Tu = 0.03\%$  and  $Tu = 0.5\%$  shows a collapse onto a single curve, reflecting good agreement with the reference data.

TABLE II. Comparison of transition parameters.

Method	$X_S/c$	$X_T/c$	$X_R/c$
$Tu = 0.03\%/Tu = 0.5\%$ <sup>5</sup>	0.03/0.03	0.15/0.13	0.29/0.23
In-house DNS <sup>32</sup>	0.02	0.16	0.27
LES <sup>55</sup>	0.02	0.16	0.27
ILES <sup>54</sup>	0.03	0.18	0.27

In Fig. 11 (b), both sets of results show a negative “trough” of  $C_f$  around  $x/c = 0.2$  for  $Tu = 0.03\%$  and around  $x/c = 0.15$  for  $Tu = 0.5\%$ , respectively, followed by the trough is the recovery to positive skin-friction values within the aft portion of the LSB. After the  $X_R/c$  point, a “crest” appears, with  $C_f$  peaking around the values of 0.003 and 0.005 for  $Tu = 0.03\%$  and  $Tu = 0.5\%$ , respectively. Note that the predicted  $C_f$  profiles sit significantly below the reference data at the crest, and a similar behavior has been observed by other researchers in their numerical studies, e.g., see<sup>8,61</sup>. There are two interesting observations: first, a shift of the predicted  $C_f$  profile in the upstream direction is observed for both  $Tu = 0.03\%$  and  $Tu = 0.5\%$ , causing a discrepancy in the aft portion of the LSB, and similar behavior has been observed by other researchers as well, see<sup>8,51,61</sup>; second, increasing freestream turbulence intensity results in earlier transition and reattachment, contributing to a reduction in the LSB length, which is consistent with the observation by Mark *et al.*<sup>62</sup> in their experimental study.

## 2. Sensitivity to $\Delta_B$

The predicted mean velocity and Reynolds shear stress profiles for eigenvalue perturbations with  $\Delta_B = 1$  for  $Tu = 0.03\%$  and  $Tu = 0.5\%$  are presented in Figs. 12 (a), (b) and 13 (a), (b), respectively. Due to the airfoil curved upper surface, both the mean velocity and Reynolds shear stress profiles are shifted down to the origin of  $y/c$ , denoted  $y/c|_o = (y - y_w)/c$  for sake of better contrast, where  $y_w$  is the vertical location of the upper surface of the airfoil. The focus of this study is on the model form uncertainty in the LSB, especially the aft portion of the LSB where noticeable discrepancies are prevalent (see Fig. 11). This is consistent with the analysis of Davide *et al.*<sup>63</sup>, whose focus was also on the aft portion of the LSB where the unstable shear layer was present with shed vortices. Two locations, i.e.,  $x/c = 0.15$  (around  $X_T$ ) and  $0.2$  (near  $X_R$ ), in the aft portion of the LSB were selected to investigate the effects of the extreme states of componentiality (1c, 2c, 3c) on both the normalized mean velocity ( $\langle U \rangle / U_\infty^2$ ) profile and normalized Reynolds shear stress ( $-\langle u_1 u_2 \rangle / U_\infty^2$ ) profile. In Figs. 12 (a) and (b), an enveloping behavior with respect to the baseline prediction is observed for both  $Tu = 0.03\%$  and  $Tu = 0.5\%$ , in the sense that the 3c perturbation reduces the magnitude of mean velocity profile, while 1c and 2c perturbations do the opposite. In addition,  $Tu = 0.03\%$  yields velocity profile that is less sensitive to the perturbations than  $Tu = 0.5\%$ , as shown in Figs. 12 (a) and (b).

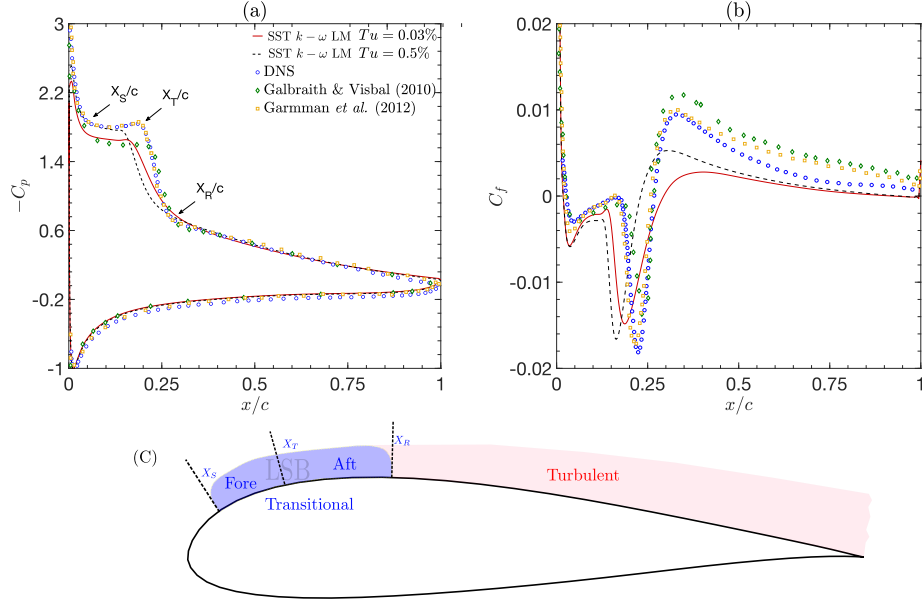


FIG. 11. Distribution of (a) pressure coefficient and (b) skin friction coefficient over a SD7003 airfoil at  $Re_c = 6 \times 10^4$  and  $AoA = 8^\circ$  for  $Tu = 0.03\%$  and  $Tu = 0.5\%$ . (c) Schematic of transitional and turbulent regions over the SD7003 airfoil with important transitional parameters highlighted.

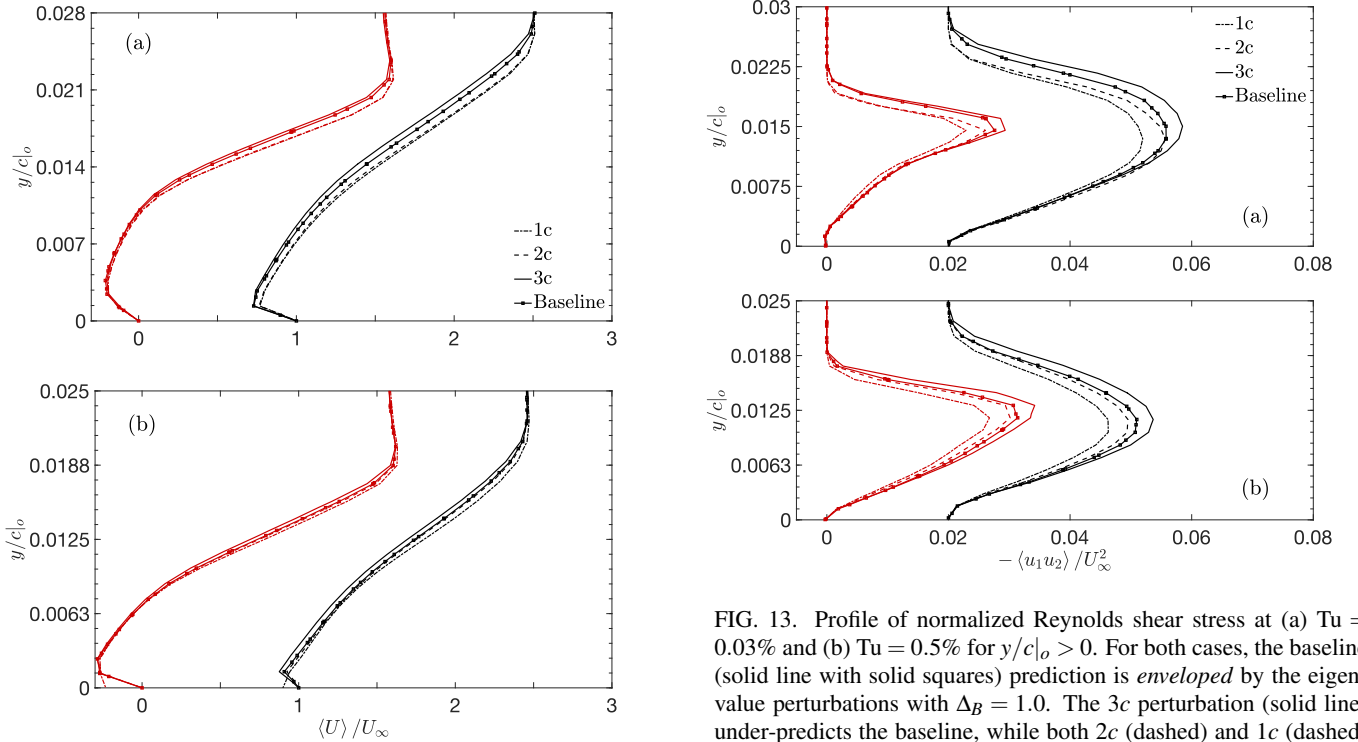


FIG. 12. Profile of normalized mean velocity at (a)  $Tu = 0.03\%$  and (b)  $Tu = 0.5\%$  for  $y/c|_o > 0$ . For both cases, the baseline (solid line with solid squares) prediction is *enveloped* by the eigenvalue perturbations with  $\Delta_B = 1.0$ . The 3c perturbation (solid line) under-predicts the baseline, while both 2c (dashed) and 1c (dashed-dotted-dashed) perturbations over-predict the baseline. From left to right are the profiles at  $x/c = 0.15$  (red) and  $x/c = 0.2$  (black).

FIG. 13. Profile of normalized Reynolds shear stress at (a)  $Tu = 0.03\%$  and (b)  $Tu = 0.5\%$  for  $y/c|_o > 0$ . For both cases, the baseline (solid line with solid squares) prediction is *enveloped* by the eigenvalue perturbations with  $\Delta_B = 1.0$ . The 3c perturbation (solid line) under-predicts the baseline, while both 2c (dashed) and 1c (dashed-dotted-dashed) perturbations over-predict the baseline. From left to right are the profiles at  $x/c = 0.15$  (red) and  $x/c = 0.2$  (black).

In Figs. 13 (a) and (b), the enveloping behavior is again observed for  $Tu = 0.03\%$  and  $Tu = 0.5\%$ . This time the 3c perturbation gives a larger value of  $-\langle u_1 u_2 \rangle / U_\infty^2$ , while the 1c and 2c perturbations do the opposite. A similar behavior

in terms of eigenvalue perturbation to the mean velocity and Reynolds shear stress profiles was observed by Luis *et al.*<sup>14</sup> as well. In addition, comparable sensitivity level to the eigenvalue perturbation is observed for  $Tu = 0.03\%$  and  $Tu = 0.5\%$ .

In Figs. 14 (a), (b), (c), (d) and 15 (a), (b), (c), (d), the predicted mean velocity normalized by the freestream velocity, and the Reynolds shear stress normalized by the freestream velocity squared,  $\langle U \rangle / U_\infty$  and  $-\langle u_1 u_2 \rangle / U_\infty^2$  for uncertainty bounds with  $\Delta_B$  in 0.25 increments, starting at 0.25 and increasing up to 1, for  $Tu = 0.03\%$  and  $Tu = 0.5\%$  and at  $x/c = 0.15$  and  $x/c = 0.2$ , respectively, are presented. It is interesting to note that both mean velocity and Reynolds shear stress show approximately linear responses to these increments in  $\Delta_B$ : a series of linear increases in the size of uncertainty bound with  $\Delta_B$  is observed. In addition, an enveloping behavior is observed for each value of  $\Delta_B$ . Overall, it shows that the increase in  $\Delta_B$  leads to more increased  $-\langle u_1 u_2 \rangle / U_\infty^2$  in magnitude compared to  $\langle U \rangle / U_\infty$ . From Figs. 14 (a), (b), (c) and (d), the sensitivity of these uncertainty bounds to  $\Delta_B$  for  $Tu = 0.03\%$  is somewhat larger than that for  $Tu = 0.5\%$ , which is consistent with the behavior shown in Figs. 12 (a) and (b). Physically, increased value of turbulence intensity suppresses the strength of eigenvalue perturbation to the Reynolds stress tensor, therefore resulting in a smaller size of uncertainty bound. In general, the simulation's response to  $\Delta_B$  is stronger for  $-\langle u_1 u_2 \rangle / U_\infty^2$  than that for  $\langle U \rangle / U_\infty$ . Therefore, it can be concluded that the degree of response to the injection of eigenvalue perturbation depends on which quantities-of-interest (QoIs) are being observed.

### 3. Visual representation for states of turbulence

Essentially, what eigenvalue perturbations do is to shift a baseline Reynolds stress anisotropy state to a new location on the barycentric map. The Reynolds stress anisotropy itself is an abstract concept, as defined in Eq. 5. This concept can be better understood if one considers barycentric map<sup>31</sup>. Figures 17 (a) - (f) show the baseline predictions for the anisotropy states using the SST  $k - \omega$  LM model at several locations selected along the suction side of the airfoil. Also included are the in-house DNS data<sup>32</sup> for comparison. In addition, Lumley's invariant map<sup>33-35</sup> as an equivalent of the barycentric map is provided for reference, as shown in Fig. 18. In addition, Fig. 16 shows the visual representations of turbulent fluctuations for the limiting states on the barycentric map and all those colorful objects are representations of the Reynolds stress ellipsoid: edges of the triangle and the three vertices of componentiality ( $1c$ ,  $2c$ ,  $3c$ ). Among them,  $1c$  (one-component) describes a flow where turbulent fluctuations only exist along one direction, referred to as "rod-like" turbulence<sup>64</sup>;  $2c$  (two-component) describes a flow where turbulent fluctuations exist along two directions, referred to as "pancake-like" turbulence<sup>64</sup>; and  $3c$  (isotropic) represents turbulence with equal fluctuations along three directions, referred to as "spherical like" turbulence<sup>64</sup>. All interior states on the barycentric map are smooth transitioning of turbulence between these limiting states.

Figures 17 (a) - (f) show Boussinesq anisotropy trajectories in a barycentric map from the wall surface ( $W_{RANS/DNS}$ ) to the outer edge of the boundary layer (OBL) ( $O_{RANS/DNS}$ ) at several locations along the suction side of the airfoil. In Figs. 17 (a) - (f), red arrow is provided to highlight the turning point where Boussinesq anisotropy state is reversing back toward  $W_{RANS}$ , i.e., the  $3c$  vertex. This indicates that the baseline RANS (SST  $k - \omega$  LM) predictions for anisotropy state tend to become more isotropic with increasing distance away from the wall. In Figs. 17 (a) - (f), the Boussinesq anisotropy states are clustered around the plane strain line. The behavior is qualitatively similar to that observed by Edeling *et al.*<sup>65</sup> and Simon D *et al.*<sup>47</sup>. Note that a simulation will follow the plane strain line if at least one eigenvalue of  $b_{ij}$  is zero<sup>31</sup>, and the Boussinesq anisotropy tensor, see Eq. 5, will give a zero eigenvalue when one of  $S_{\alpha\alpha}$  equals zero. Therefore, all two-dimensional simulations will yield anisotropy trajectories along the plane strain when the Boussinesq turbulent viscosity hypothesis is adopted, i.e.,  $\hat{b}_{ij} = \text{diag}(\lambda_1, 0, -\lambda_1)$ . This behavior was also observed by Edeling *et al.*<sup>65</sup> and Simon *et al.*<sup>47</sup>. Overall, the SST  $k - \omega$  LM anisotropy states are more isotropic.

More interestingly, DNS yields realistic anisotropy states. For the aft portion of the LSB, Fig. 17 (a) shows that DNS produces turbulence in axisymmetric contraction state at the wall for  $x/c = 0.015$ , shifting to an axisymmetric expansion state and then reversing back toward the axisymmetric contraction state at the OBL. Refer to Fig. 16, this indicates that turbulence exhibits an oblate spheroid at the wall, then gradually transitions to a prolate spheroid, and eventually exhibits an oblate spheroid at the OBL. A similar behavior is observed at  $x/c = 0.2$  as well, as shown in Fig. 17 (b). This indicates that the laminar-turbulent transition process tends to suppress the streamwise stresses in the regions both close to the wall and in the outer region of the boundary layer, while fosters the streamwise stresses in between. Within the attached turbulent boundary layer from  $x/c = 0.3$  to  $0.6$ , there is a tendency for turbulence at the wall to shift from the axisymmetric contraction state to the two-component state (wall-normal Reynolds stresses damped out at the wall); while away from the wall turbulence gradually shifts toward the axisymmetric expansion, reflecting increased streamwise stresses. Figures 18 (a) - (f) present anisotropy trajectories in the Lumley's invariant map, which contain the same information as the barycentric map, except based on a non-linear domain (non-linearity in variables  $II$  and  $III$ ). Overall, same trend is observed using the Lumley's invariant map; however clusters of anisotropy states appear around the  $3c$  vertex.

Because anisotropy states are defined based on  $\lambda_i$ , its trajectories do not contain information regarding the physical domain<sup>64</sup>. This shortcoming is addressed by painting the points based on physical coordinates, as shown in Figs. 19 (a) - (d). Figures 19 (a) - (d) present the anisotropy states for all locations on both the barycentric map and the Lumley's invariant map, respectively. Overall, the Boussinesq anisotropy states are more isotropic, clustering around the plane strain line, as shown in Figs. 19 (a) and (c). On the other hand, the DNS anisotropy states scatter on both maps, reflecting

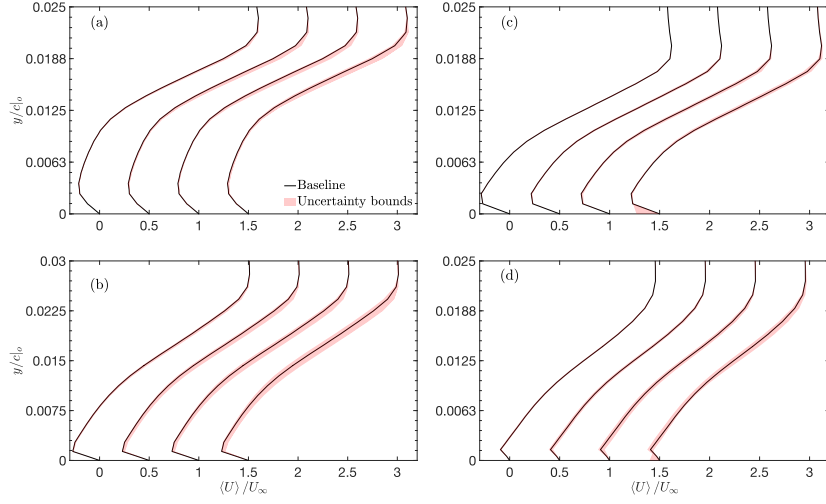


FIG. 14. Profile of normalized mean velocity at (a)  $x/c = 0.15$  and (b)  $x/c = 0.2$  for  $Tu = 0.03\%$ ; profile of normalized mean velocity at (c)  $x/c = 0.15$  and (d)  $x/c = 0.2$  for  $Tu = 0.5\%$ . Uncertainty bounds, i.e., red region between  $1c$  and  $3c$  eigenvalue perturbations, with different magnitudes of  $\Delta_B$  are displayed. From left to right are  $\Delta_B = 0.25, 0.5, 0.75$ , and  $1.0$  perturbations, respectively. The unperturbed baseline prediction (solid line) is provided for reference.

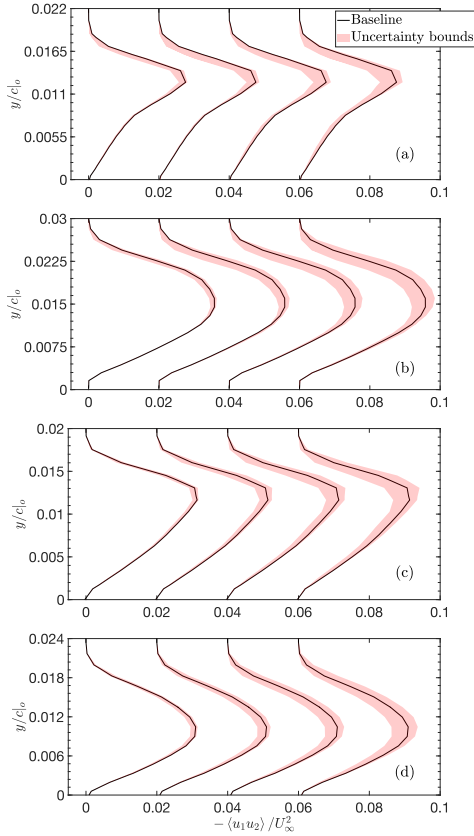


FIG. 15. Profile of normalized Reynolds shear stress at (a)  $x/c = 0.15$  and (b)  $x/c = 0.2$  for  $Tu = 0.03\%$ ; (c) profile of normalized Reynolds shear stress at (c)  $x/c = 0.15$  and (d)  $x/c = 0.2$  for  $Tu = 0.5\%$ . Uncertainty bounds with different magnitudes of  $\Delta_B$ , i.e., red region between  $1c$  and  $3c$  profiles, are displayed. From left to right are  $\Delta_B = 0.25, 0.5, 0.75$ , and  $1.0$  perturbations. The unperturbed baseline prediction (solid line) is provided for reference.

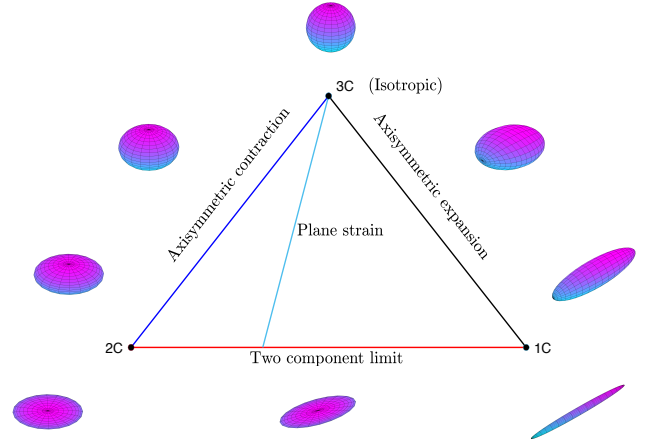


FIG. 16. Shapes of limiting anisotropy states in the barycentric map corresponding to varying componentiality of the flow: one-component ( $1c$ ), two-component ( $2c$ ), and three-component ( $3c$ ), which are joint by three limiting boundary states (axisymmetric contraction, axisymmetric expansion, and two-component limit). Note that the axisymmetric contraction and expansion states describe turbulent fluctuations in the shape of oblate and prolate spheroids, respectively.

a tendency of turbulence shifting from more axisymmetric contraction/two-component (oblate spheroid or pancake-like) to axisymmetric expansion (prolate spheroid) when the distance from the wall is increased, as shown in Figs. 19 (b) and (d).

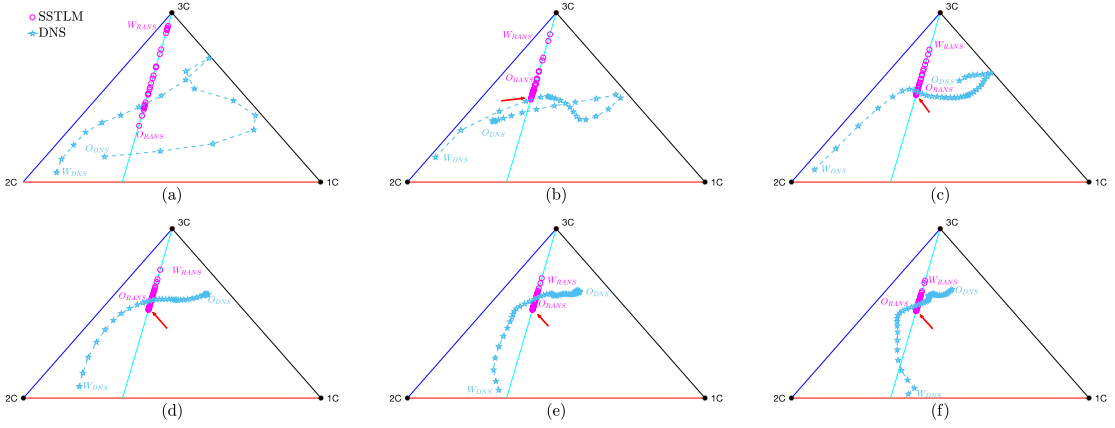


FIG. 17. Anisotropy states based on eigenvalues of anisotropy tensor for Reynolds stress on the barycentric map<sup>31</sup> for  $Tu = 0.03\%$ . (a) - (c):  $x/c = 0.15, 0.2$  and  $0.3$ . (d) - (e):  $x/c = 0.4, 0.5$  and  $0.6$ . Anisotropy trajectory follows the path from  $W_{RANS/DNS}$  (at the wall) to  $O_{RANS/DNS}$  (OBL). Red arrows are added to indicate the point at which the SST  $k - \omega$  LM trajectories reverse back in the opposite direction toward  $W_{RANS}$  along the plane strain line.

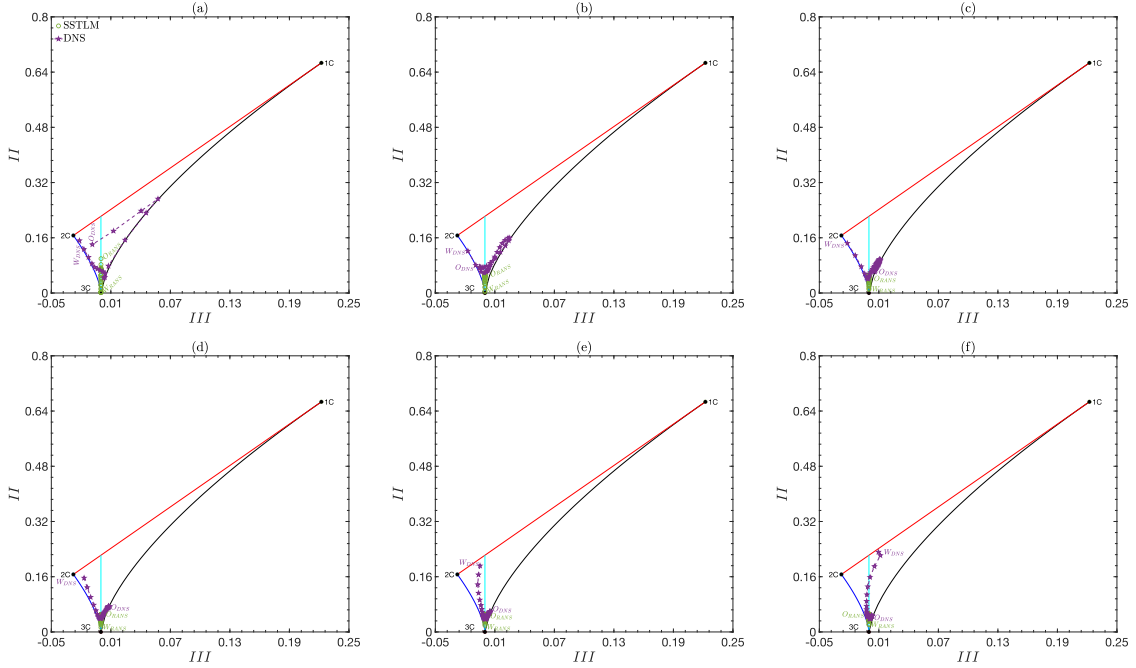


FIG. 18. Anisotropy states characterized by invariants ( $II, III$ ) of anisotropy tensor for Reynolds stress on the Lumley's invariant map<sup>33</sup> for  $Tu = 0.03\%$ . (a) - (c):  $x/c = 0.15, 0.2$  and  $0.3$ . (d) - (e):  $x/c = 0.4, 0.5$  and  $0.6$ . Anisotropy trajectory follows the path from  $W_{RANS/DNS}$  (at the wall) to  $O_{RANS/DNS}$  (OBL).

#### 4. Instantaneous velocity field

The unsteady visualization of ‘‘vortex shedding’’<sup>66</sup> from the baseline and the eigenvalue perturbations of  $1c$  and  $3c$  are presented in Fig. 20. Energy losses are accompanied with a vortex shedding phenomenon that involves high unsteadiness within the flow<sup>67–71</sup>. Streamlines are provided to capture the shed vortices on the suction side of the airfoil. Figure 20 shows the snapshots of the flow at four different times:  $T_0$ ,  $T_1$ ,  $T_2$ , and  $T_3$ . The shed vortices convect downstream, and even-

tually breakdown to smaller structures<sup>63,72</sup>. All simulations show that the LSB first originates at  $T_0$  for  $0.3 < x/c < 0.6$ , then gradually moves nearer to the leading edge at  $T_3$ . In Fig. 20, vortex paring begins at  $T_1$ , and the coalesced vortices become a single, larger vortex at  $T_2$ , which significantly increases the boundary layer thickness, and similar behavior has been observed by other researchers<sup>63,73</sup> as well. This large-scale vortex or coherent structure<sup>63</sup> remains near the leading edge, followed by vortex shedding breaking down to turbulence further downstream. Note that this large-scale vortex

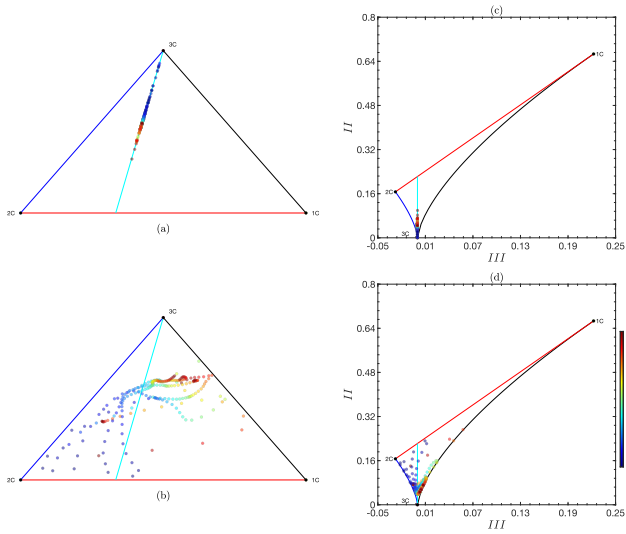


FIG. 19. Anisotropy states for  $x/c = 0.15, 0.2, 0.3, 0.4, 0.5$  and  $0.6$  on both the barycentric and Lumley's invariant maps. (a) and (c): SST  $k - \omega$  LM simulation ( $Tu = 0.03\%$ ); (b) and (d): in-house DNS. Note that anisotropy states are painted based on the distance from the wall surface.

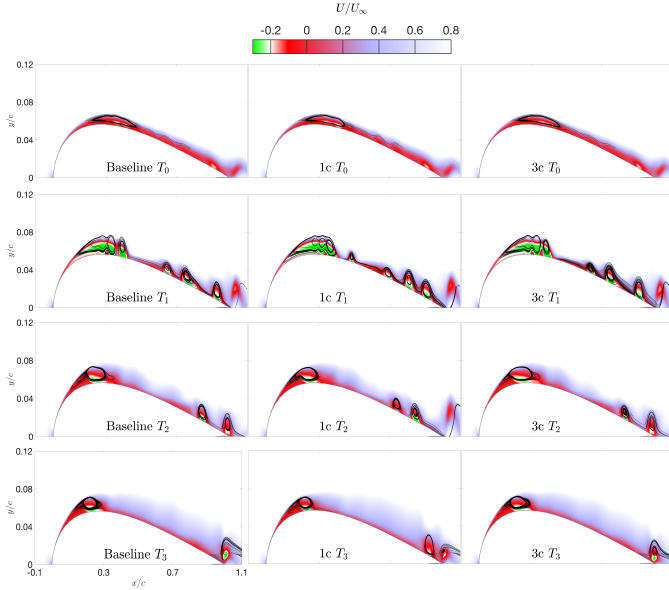


FIG. 20. Contours of initial transient behavior of instantaneous mean streamwise velocity for baseline and eigenvalue perturbations ( $1c$  and  $3c$ ) at different times:  $T_0 = 0.1, T_1 = 0.13, T_2 = 0.15, T_3 = 0.17$ . Streamlines are superimposed on the plot to capture the vortex shedding process.  $Tu = 0.03\%$ .

structure indicates the evolution of a LSB at an early stage. At  $T_3$ , the turbulence downstream is composed of stochastic small-scale structures, which are smeared out by the unsteady SST  $k - \omega$  LM model. Compared to the baseline prediction, the  $1c$  perturbation tends to suppress the size of the coherent structure near the leading edge, while the  $3c$  perturbation tends to bolster the size of it, as can be seen at  $T_3$ .

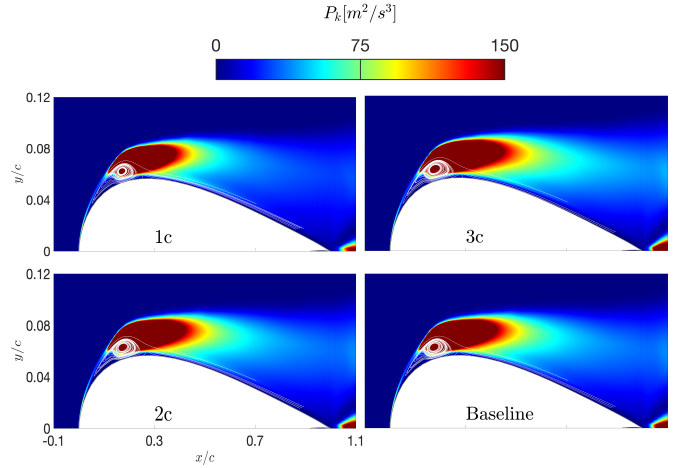


FIG. 21. Contours of turbulent production for  $1c, 2c$  and  $3c$  perturbations at  $Tu = 0.03\%$ . Baseline prediction is provided for reference. Streamlines show the size of the LSB on the suction side of the airfoil.

### 5. Turbulent production

Figure 21 shows contours of turbulent production from the baseline and the  $1c, 2c,$  and  $3c$  perturbations. Also included are the time-averaged streamlines to highlight the location for reverse flow incurred within the LSB. In Fig. 21, values of  $P_k$  appear to be very small, i.e., close to zero, in the vicinity of the wall near the leading edge  $x/c < 0.15$ , and in the outer region of the flow as well. This suggests a low level of turbulence is produced in these regions, where mean-flow kinetic energy is more prevalent. From Fig. 21, for all contour plots it clearly shows a peak of  $P_k$  found in the dark red region where the LSB is present, and the level of  $P_k$  gradually deteriorates downstream. In addition, the  $1c$  perturbation produces a smaller value of  $P_k$  than the baseline prediction. On the other hand, the  $3c$  perturbation produces a larger value of  $P_k$  than the baseline prediction. This behavior is qualitatively similar to the very recent study of Clara *et al.*<sup>60</sup>, which focused on enhancing the turbulent production in the LSB. On the other hand,  $P_k$  produced by the  $2c$  perturbation has a comparable magnitude to that for the baseline prediction, and hence in between the  $1c$  and  $3c$  perturbations.

### 6. Skin friction coefficient

The baseline prediction along with the eigenvalue perturbations ( $1c, 2c, 3c$ ) for  $C_f$  are shown in Figs. 22 (a), (c) ( $Tu = 0.03\%$ ), (b), (d) ( $Tu = 0.5\%$ ). Also included are the in-house DNS<sup>32</sup> and ILES/LES data by<sup>54</sup> and<sup>55</sup> for comparison.

Figures 22 (a) and (b) enlarge the region for the trough to distinguish the clusters of  $C_f$  profiles, where a negative peak is present around  $x/c = 0.2$ . In this region, a trough of  $C_f$  appears, reflecting the significantly increased  $C_f$  in magnitude

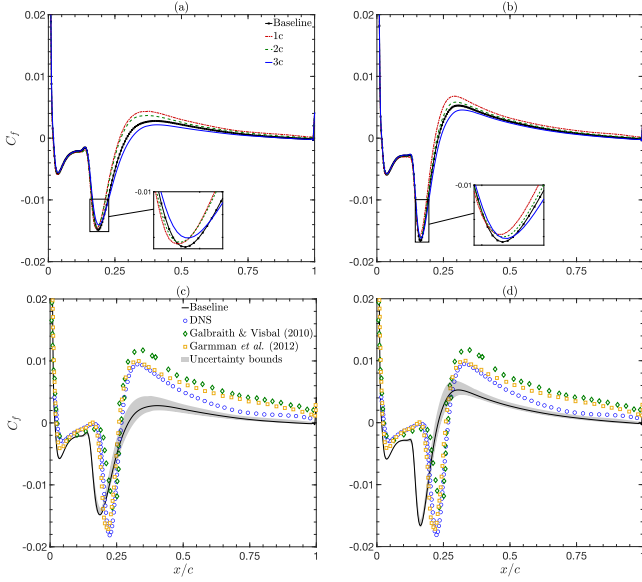


FIG. 22. Distribution of skin friction coefficient for  $1c$ ,  $2c$  and  $3c$  perturbations with enlarged region at trough and uncertainty bounds for eigenvalue perturbations with uniform value of  $\Delta_B = 1$ : (a) and (c) for  $Tu = 0.03\%$ , (b) and (d) for  $Tu = 0.5\%$ . Baseline prediction is provided for reference.  $\circ$  in-house DNS data<sup>32</sup>.

within the LSB. In this region, enveloping behavior with respect to the baseline prediction occurs except around the negative peak in the trough, where the  $1c$  perturbation sits slightly below the baseline prediction, while the  $3c$  perturbation sits somewhat above the baseline prediction. A similar behavior has been observed by Mishra and Iaccarino<sup>12</sup> and Iaccarino *et al.*<sup>13</sup> in their UQ study for the canonical case of a turbulent flow over a backward-facing step. Downstream of the peak, the value of  $C_f$  begins to sharply recover and approaches a value of  $C_f = 0$  near  $X_R$ . In the recovery region, the  $1c$  and  $2c$  perturbations sit above the baseline prediction while the  $3c$  perturbation does the opposite, indicating a reduction of  $C_f$  for the  $1c$  and  $2c$  perturbations (enhancing  $\langle U \rangle$ ), while an increase of  $C_f$  for the  $3c$  perturbation (suppressing  $\langle U \rangle$ ) in the aft portion of the LSB. This is consistent with the behavior of the perturbed  $C_f$  for T3A with the SST  $k - \omega$  LM model, as shown in Fig. 8. As a consequence, shortening of the LSB length is observed under the  $1c$  and  $2c$  perturbations, which leads to an upstream shift of  $X_R$  and shows a tendency to approach closer to the reference data. On the other hand, the  $3c$  perturbation shifts the  $X_R$  point further downstream, resulting in a larger length LSB. A similar behavior has been observed by other researchers in their numerical studies for the canonical case of a turbulent flow over a backward-facing step, e.g., see<sup>11-13</sup>.

Further downstream of  $X_R$  is the attached turbulent boundary layer, where the  $1c$  and  $2c$  perturbations sit consistently above the baseline prediction, while the  $3c$  perturbation does the opposite but in a less intense manner. In addition, these three eigenvalue perturbations gradually approach the baseline prediction as the flow moves further downstream of

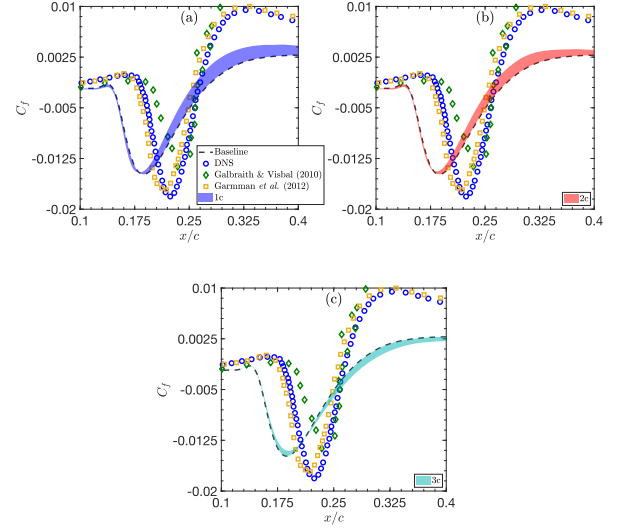


FIG. 23. Enlarged version of Fig. 22 (c) ( $Tu = 0.03\%$ ) at trough. Displayed are the uncertainty bounds for (a)  $1c$ , (b)  $2c$  and (c)  $3c$  perturbations. Baseline prediction is provided for reference.  $\circ$  in-house DNS data<sup>32</sup>.

$X_R$ . This indicates that the model form uncertainty becomes smaller as the flow proceeds further downstream, hence an increase in trustworthiness in the baseline prediction. In Figs. 22 (c) and (d), the uncertainty bounds ( $1c$ ,  $2c$ ,  $3c$ ) depicted by the gray region are constructed with respect to the baseline prediction. In the fore portion of the LSB, it is clear that negligibly small responses to  $1c$ ,  $2c$  and  $3c$  perturbations are observed for the region  $x/c < 0.15$ , collapsing onto the baseline prediction and indicating relatively high trustworthiness, i.e., showing relatively good agreement with the in-house DNS<sup>32</sup> and ILES/LES data of<sup>54,55</sup>. However, the size of the uncertainty bounds begins to increase in the aft portion of the LSB (further downstream of  $X_T$ ). Figure 22 (c) clearly shows that the uncertainty bounds encompass  $X_R$  based on the in-house DNS and ILES/LES data of<sup>54,55</sup> for  $Tu = 0.03\%$ . On the other hand, an overall shift in the upstream direction is observed for  $Tu = 0.5\%$ , failing to encompass  $X_R$ . Downstream of  $X_R$ , a noticeable discrepancy is observed for both  $Tu = 0.03\%$  and  $Tu = 0.5\%$ , and uncertainty bounds are insufficient to encompass the reference data. In addition, the size of the uncertainty bounds for  $Tu = 0.5\%$  is overall smaller than that for  $Tu = 0.03\%$ , as shown in 22 (d). The important conclusion is that the simulation's response to the injection of eigenvalue perturbation varies with the magnitude of initial turbulent condition being used.

Figures 23 (a) - (c) enlarge the region for the trough to highlight the individual effects of these eigenvalue perturbations ( $1c$ ,  $2c$ ,  $3c$ ) for  $Tu = 0.03\%$ . In the fore portion of the LSB ( $0.02 < x/c < 0.15$ ), all of the eigenvalue perturbations and the baseline prediction collapse onto a single curve, indicating a low sensitivity to the injection of eigenvalue perturbation and hence low level of model form uncertainty. On the

other hand, the uncertainty bounds for  $1c$  and  $2c$  sit above the baseline prediction, reflecting a decrease in magnitude, with  $2c$  less strength than  $1c$ , in the aft portion of the LSB ( $0.15 < x/c < 0.26$ ). This contributes to a reduction of the discrepancy at the crest (the aft portion of the LSB), as shown in Figs. 23 (a) and (b). In contrast to  $1c$  and  $2c$  perturbations,  $3c$  perturbation sits somewhat below the baseline prediction, giving a lower value of  $C_f$ , while in a weaker strength (smaller size of the uncertainty bound) compared to the  $1c$  and  $2c$  perturbations. Because  $3c$  perturbation retains the isotropic nature of the turbulent viscosity model, it has limited effect on the perturbed results. This explains the smaller size of uncertainty bound generated from the  $3c$  perturbation compared to the  $1c$  and  $2c$  perturbations. Such inefficacy of  $3c$  perturbation has been observed by Emory *et al.*<sup>9</sup> as well. As the result, this increases the discrepancy by deviating away from the reference data.

## 7. Pressure coefficient

Figures 24 (a), (c) ( $Tu = 0.03\%$ ), (b), (d) ( $Tu = 0.5\%$ ) present the distribution of pressure coefficient  $C_p$  over the SD7003 airfoil: baseline prediction and eigenvalue perturbations ( $1c$ ,  $2c$ ,  $3c$ ). The in-house DNS<sup>32</sup> and ILES/LES data of<sup>54</sup> and<sup>55</sup> are included for comparison. In Figs. 24 (a) and (b), the region at the flat spot where the laminar-turbulent transition process occurs is enlarged. In this region, the  $1c$  and  $2c$  perturbations lie somewhat above the baseline prediction, with  $2c$  less strength than  $1c$ . On the other hand, the  $3c$  perturbation shows comparable strength with the  $1c$  perturbation, lying below the baseline prediction, as shown in Figs. 24 (a) and (b). Except for the flat spot, all of the profiles show a collapse, indicating a type of similarity.

In Figs. 24 (c) and (d), the uncertainty bounds ( $1c$ ,  $2c$ ,  $3c$ ) depicted by the gray region are constructed with respect to the baseline prediction, and no discernible uncertainty bounds is observed except at the flat spot, which is within the fore portion of the LSB. In addition, an enveloping behavior with respect to the baseline prediction is observed at the flat spot. This indicates that the model form uncertainty is most prevalent at the flat spot, indicating relatively low trustworthiness in the prediction for  $C_p$ . It is interesting to note that the uncertainty bounds for  $Tu = 0.03\%$  tend to encompass the ILES data of<sup>54</sup> at the flat spot, while the uncertainty bounds for  $Tu = 0.5\%$  tend to encompass the in-house DNS<sup>32</sup> and LES data of<sup>55</sup>. These trends do not happen in the prediction for  $C_f$ , as shown in Fig. 22. In the aft portion of the LSB, a small discrepancy that marks a lower value of  $C_p$  is observed except in the region around  $X_R$ , where it gives a slightly larger value of  $C_p$ . On the other hand, no discernible uncertainty bounds is observed for the rest regions, reflecting a low level of the model form uncertainty and hence relatively high trustworthiness. Overall, the size of the uncertainty bounds for  $Tu = 0.03\%$  is larger than that for  $Tu = 0.5\%$ . This again confirms the conclusion drawn previously: the degree of response to the injection of eigenvalue perturbation varies with the magnitude of initial turbulent condition being used. There

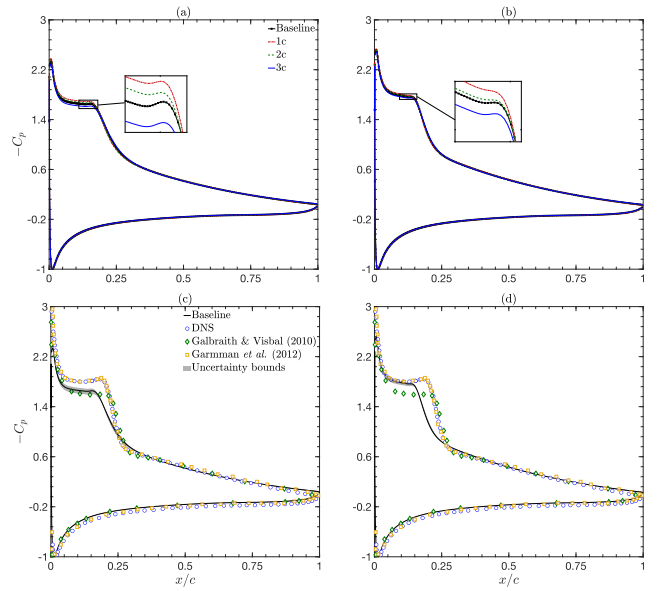


FIG. 24. Distribution of pressure coefficient for  $1c$ ,  $2c$  and  $3c$  perturbations with enlarged region at flat spot and uncertainty bounds for eigenvalue perturbations with uniform value of  $\Delta_B = 1$ : (a) and (c) for  $Tu = 0.03\%$ , (b) and (d) for  $Tu = 0.5\%$ . Baseline prediction is provided for reference.  $\circ$  in-house DNS data<sup>32</sup>.

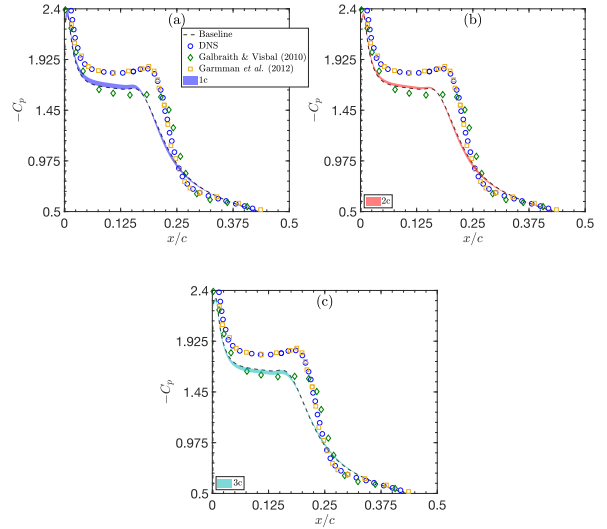


FIG. 25. Enlarged version of Fig. 24 (c) ( $Tu = 0.03\%$ ) at flat spot. Displayed are the uncertainty bounds for (a)  $1c$ , (b)  $2c$  and (c)  $3c$  perturbations. Baseline prediction is provided for reference.  $\circ$  in-house DNS data<sup>32</sup>.

is an important observation:  $C_p$  is clearly much less sensitive to the eigenvalue perturbations than  $C_f$ , as shown in Figs. 22 (c) and (d). The perturbed  $C_p$  profiles only deviates from the baseline prediction at the flat spot. This is due to the fact that the wall pressure is determined by the freestream, which is only modified meticulously by the eigenvalue perturbations<sup>9</sup>.



Figures 25 (a) - (c) enlarge the region for the flat spot to highlight the individual effects of these eigenvalue perturbations ( $1c$ ,  $2c$ ,  $3c$ ) for  $Tu = 0.03\%$ . Figures 25 (a) and (b) show that the uncertainty bound for  $1c$  over-predicts the baseline prediction more than that for  $2c$  at the flat spot, while  $3c$  does the opposite in a comparable strength to the  $1c$  perturbation. As a result, a tendency for  $1c$  and  $2c$  to approach toward the in-house DNS<sup>32</sup> and LES data of<sup>55</sup>, and  $3c$  to approach closer to the ILES data of<sup>55</sup>, is observed at the flat spot, as shown in Figs. 25 (a) - (c).

## 8. Mean velocity field

Contours of the mean velocity normalized with the freestream velocity,  $\langle U \rangle / U_\infty$  from the baseline, eigenvalue perturbations ( $1c$ ,  $2c$ ,  $3c$ ), and in-house DNS of<sup>32</sup> in an  $xy$  plane are shown in Fig. 26. Moreover, included mean streamlines for the depiction of reverse flow ( $\langle U \rangle / U_\infty < 0$ ) clearly show a large recirculating region located upstream in the region near the leading edge. The large recirculating region contains large-temporal-scale events (coherent structures), which are at low-frequency fluctuations due to very-large scale of unsteadiness of the recirculating region itself<sup>74</sup>. Consequently, these large-scale coherent structures survive after time-averaging, namely LSB. The contours confirm the behavior observed in the prediction for  $C_f$ . First, the  $1c$  and  $2c$  perturbations reduce the magnitude of  $C_f$  in the aft portion of the LSB compared to the baseline prediction, which leads to a lower value of  $P_k$  shown in Fig. 21, indicating subdued turbulence. Second, the  $3c$  perturbation does the opposite, i.e., increased magnitude of  $C_f$  bolstering  $P_k$  and hence an increase in turbulence kinetic energy in the aft portion of the LSB. Recall that turbulence is produced through the straining mechanism,  $(-\langle u_i u_j \rangle \frac{\partial \langle U_i \rangle}{\partial x_j})$ , i.e., a transfer of kinetic energy from mean flow to turbulence<sup>34,35</sup>. Therefore, the  $1c$  and  $2c$  perturbations that enhance the streamwise stresses working against the mean flow gradient in a sense of reversal of energy from turbulence to the mean field have redistributed the flow energy in the LSB, while the  $3c$  perturbation enhances the mechanism of transferring kinetic energy from the mean flow to turbulence. Correspondingly, the  $1c$  and  $2c$  perturbations increase the magnitude of  $\langle U \rangle / U_\infty$  as a compromise to the decrease of the turbulence kinetic energy contained in the LSB, while the  $3c$  perturbation reveals an reduction in the magnitude of  $\langle U \rangle / U_\infty$  to bolster turbulence. As a result, it can be observed that the size of the region of reverse flow becomes smaller for  $1c$  and  $2c$  compared to the baseline prediction, characterized by a shallower region of streamlines, while  $3c$  gives a larger size of the region of reverse flow, characterized by a broader region of streamlines. As the flow approaches downstream of  $X_R$ , streamlines for  $1c$  and  $2c$  get closer than that for the baseline prediction, indicating a larger magnitude of  $\langle U \rangle / U_\infty$ , while streamlines for  $3c$  get thinner, which reflects a smaller magnitude of  $\langle U \rangle / U_\infty$ , as shown in Fig. 26. In addition, the  $2c$  perturbation yields a magnitude of  $\langle U \rangle / U_\infty$  in between the  $1c$  and  $3c$  perturbations. In comparison to the baseline predic-

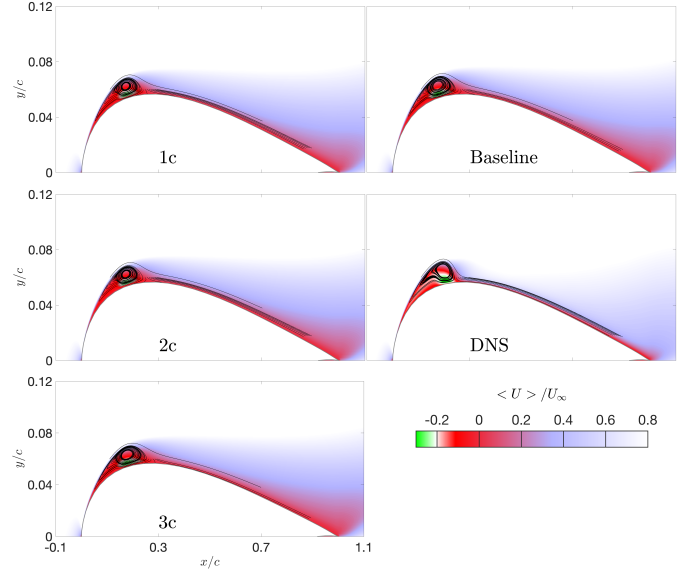


FIG. 26. Contours of  $\langle U \rangle / U_\infty$  for  $1c$ ,  $2c$  and  $3c$  perturbations at  $Tu = 0.03\%$ . Baseline prediction is provided for reference, and in-house DNS data<sup>32</sup> are included for comparison. Streamlines show the size of the LSB on the suction side of the airfoil.

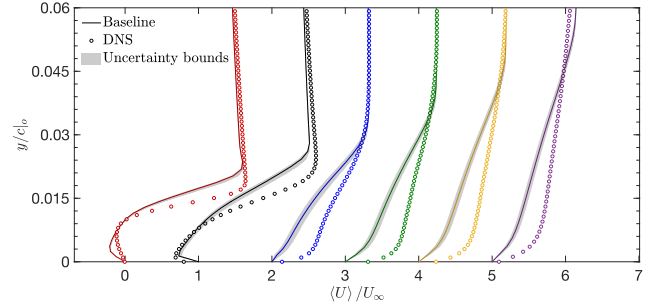


FIG. 27. Streamwise mean velocity profiles in the aft portion of the LSB ( $x/c = 0.15$  and  $0.2$ ) and in the attached turbulent boundary layer ( $x/c = 0.3, 0.4, 0.5$  and  $0.6$ ) at  $Tu = 0.03\%$ . From left to right are  $x/c = 0.15, 0.2, 0.3, 0.4, 0.5$  and  $0.6$ , respectively. Displayed are uncertainty bounds for eigenvalue perturbations with uniform value of  $\Delta_B = 1$  ( $1c$ ,  $2c$  and  $3c$ ). Baseline prediction is provided for reference.  $\circ$  in-house DNS data<sup>32</sup>.

tion, the in-house DNS data overall show a larger magnitude of  $\langle U \rangle / U_\infty$  in the attached turbulent boundary layer. This is characterized by the densely piled-up streamlines next to the wall, showing similar behavior to the  $1c$  and  $2c$  perturbations. Moreover, a larger region of reverse flow is observed for the in-house DNS data than that for the baseline prediction, and hence a larger recirculating vortex formed, depicted by the mean streamlines. As the height of the LSB produced by in-house DNS is somewhat increased compared to the baseline prediction, which modifies the effective shape of the SD7003 airfoil<sup>56</sup>. This might partly explain the discrepancies that appear in the baseline predictions for  $C_f$  and  $C_p$ .

The predicted mean  $\langle U \rangle / U_\infty$  profiles across the entire boundary layer on the suction side are plotted in Fig. 27. The

uncertainty bounds generated from the eigenvalue perturbations ( $1c$ ,  $2c$ ,  $3c$ ) are depicted by gray regions, as shown in Fig. 27. Also included is the in-house DNS data of<sup>32</sup>. The boundary layer has separated in the aft portion of the LSB at  $x/c = 0.15$  and  $0.2$ , where the reverse flow close to the wall is visible. At  $x/c = 0.15$ , the predicted  $\langle U \rangle / U_\infty$  profile shows good agreement with the in-house DNS data for  $0.006 < y/c < 0.012$  and  $y/c > 0.021$ , except in the region next to the wall  $y/c < 0.006$  and far from the wall  $0.012 < y/c < 0.021$ . The response to the injection of eigenvalue perturbation for  $x/c = 0.15$  is negligibly small, and no encompassing of the in-house DNS data is observed. As the flow moves a bit further downstream, the uncertainty bounds tend to encompass the in-house DNS data in the region of reverse flow next to the wall  $y/c < 0.012$ , while a growing discrepancy is found gradually away from the wall  $0.012 < y/c < 0.027$ , and no discernible uncertainty bounds is observed above the OBL  $y/c > 0.027$ . Further downstream of  $X_R$  is the attached TBL (from  $x/c = 0.3$  to  $x/c = 0.6$ ), the recovery to turbulent profile occurs, showing consistent under-predictions for the  $\langle U \rangle / U_\infty$  profiles. A similar behavior was observed by Luis *et al.*<sup>61</sup> in their numerical study for a transitional flow over a NACA 0012 airfoil using the SST  $k - \omega$  LM model. This is due to the inaccurate prediction for the period vortical structures that shed downstream. The uncertainty bound reduces in size as the flow proceeds from  $x/c = 0.3$  to  $x/c = 0.6$ . The positive values of  $C_f$  after  $X_R$  might partly contribute this behavior. Moreover, it should be noted that the SST  $k - \omega$  LM model is inherently incapable of capturing the presence of rotational strains due to the adoption of the Boussinesq turbulent viscosity hypothesis. However, rotation strains make crucial contributions to the evolution of turbulence. For example, on the cambered SD7003 airfoil the boundary layer growth rate is decreased on the convex surface and increased on the concave surface. However, the eigenspace perturbation method strictly adheres to the extended form of the Boussinesq turbulent viscosity hypothesis, therefore is unable to account for the limitations of rotation and curvature effects<sup>45</sup>. This might partly explain the insufficient uncertainty bounds to encompass the discrepancies observed in Figs. 23 and 27.

Figures 28 (a) - (r) expand the near-wall region to highlight the individual effects of eigenvalue perturbations ( $1c$ ,  $2c$ ,  $3c$ ) on  $\langle U \rangle / U_\infty$ . At  $x/c = 0.15$ , Figs. 28 (a) and (b) show that the  $1c$  and  $2c$  perturbations tend to over-predict the baseline prediction, although very slightly. On the other hand, the  $3c$  perturbation becomes almost indistinguishable from the baseline prediction, as shown in Fig. 28 (c). At  $x/c = 0.2$ , the uncertainty bounds generated from the  $1c$  and  $2c$  perturbations are noticeably increased in size, sitting below the baseline prediction. On the other hand, the simulation is less sensitive to the  $3c$  perturbation, yielding a relatively small uncertainty bound that sits above the baseline prediction, as shown in Figs. 28 (d) - (f). From  $x/c = 0.3$  to  $x/c = 0.6$ , the flow begins to recover to turbulent profile, the size of the uncertainty bounds generated from the  $1c$ ,  $2c$ , and  $3c$  perturbations increases to maximum at  $x/c = 0.3$ , followed by a steady decrease further downstream. Overall, it is clear that the  $1c$  and  $2c$  uncertainty bounds over-predict the baseline prediction, showing a ten-

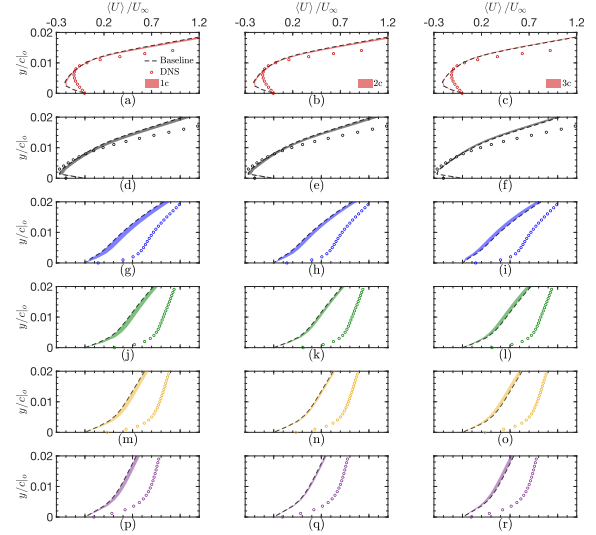


FIG. 28. Enlarged version of Fig. 27 for region next to the wall  $0 < y/c|_o < 0.02$ . From top to bottom are (a), (b), (c) for  $x/c = 0.15$ , (d), (e), (f) for  $x/c = 0.2$ , (g), (h), (i) for  $x/c = 0.3$ , (j), (k), (l) for  $x/c = 0.4$ , (m), (n), (o) for  $x/c = 0.5$  and (p), (q), (r) for  $x/c = 0.6$ , respectively. From left to right are  $1c$ ,  $2c$  and  $3c$  perturbation results, displaying a clear relationship between which perturbation and the size of its uncertainty bound. Baseline prediction is provided for reference.  $\circ$  in-house DNS data<sup>32</sup>.

dency to approach closer to the in-house DNS data, while the  $3c$  uncertainty bound does the opposite. A similar behavior was also observed by Luis *et al.*<sup>14</sup> in their numerical study for a turbulent flow over a backward-facing step. Moreover, it should be noted that the  $1c$  and  $2c$  perturbations react more favorably with the positive  $C_f$  values in the region downstream of  $X_R$  than the  $3c$  perturbation, characterized by a rather noticeable decrease in the size of the uncertainty bounds.

## 9. Reynolds shear stress

Contours of the Reynolds shear stress normalized with the freestream velocity squared,  $-\langle u_1 u_2 \rangle / U_\infty^2$  from the baseline,  $1c$ ,  $2c$  and  $3c$  perturbations, and in-house DNS<sup>32</sup> in an  $xy$  plane are shown in Fig. 29. Streamlines are included to depict the region of reverse flow, where the LSB is present. From Fig. 29, it is clear that the magnitude of  $-\langle u_1 u_2 \rangle / U_\infty^2$  is almost zero in the region near the leading edge as well as in the outer region of the flow. A similar behavior was observed by Zhang and Rival<sup>75</sup> in their experimental study. Recall that the Reynolds shear stress is dedicated to the contribution of the turbulent production<sup>34,35</sup>, a low level of turbulence should be produced in these regions. This confirms the behavior observed in the prediction for  $P_k$  shown in Fig. 21. In addition, Fig. 29 shows that  $-\langle u_1 u_2 \rangle / U_\infty^2$  contours are everywhere positive, which is consistent with the positive magnitude of turbulent production observed in Fig. 21 (the correlation  $\langle u_1 u_2 \rangle$  is

almost always negative when the mean gradient is positive, and vice versa). Likewise, the magnitude of  $-\langle u_1 u_2 \rangle / U_\infty^2$  reduces as the flow approaches further downstream from the LSB where a peak value of  $-\langle u_1 u_2 \rangle / U_\infty^2$  is found, i.e., bright yellow region for  $x/c \sim 0.25$ . It should be noted that the highest Reynolds shear stress happens around  $X_R$ , where a high level of momentum transfer due to anisotropy Reynolds stresses is present. A similar behavior was observed in the experimental measurements of Zhang and Rival<sup>75</sup> as well. From Fig. 29, the  $1c$  and  $2c$  perturbations under-predict the baseline prediction, with  $2c$  yielding a relatively larger magnitude of  $-\langle u_1 u_2 \rangle / U_\infty^2$  than that for  $1c$ , while the  $3c$  perturbation over-predicts the baseline prediction. In addition, it clearly shows that the baseline prediction for the  $-\langle u_1 u_2 \rangle / U_\infty^2$  contour is prominently reduced in magnitude compared to the in-house DNS data across the entire suction side. Therefore, the  $3c$  perturbation that increases the magnitude of  $-\langle u_1 u_2 \rangle / U_\infty^2$  shows a tendency of approaching closer to the in-house DNS data, which is consistent with the behavior of the prediction for  $P_k$  shown in Fig. 21. One may notice that the  $3c$  perturbation with the largest turbulent production does not have the reattachment point occur earlier than the  $1c$  perturbation with the least turbulent production. According to Davide *et al.*<sup>63</sup>, the overall turbulence kinetic energy can be decomposed into the large-scale coherent (Kelvin-Helmholtz induced) and stochastic (turbulence-induced) contributions. The  $1c$  perturbation suppresses the size of the LSB, during which part of the coherent energy is reversed into the mean flow. On the other hand, the  $3c$  perturbation fosters the large-scale coherent vortex-shedding structures by extracting more energy from the mean flow, which results in large coherent energy stored in these large-scale structures. This might partly explain the anomalous behavior. The similar behavior has been observed by Gianluca *et al.*<sup>13</sup> and Luis *et al.*<sup>14</sup> in their numerical study for a turbulent flow over a backward-facing step.

The predicted  $-\langle u_1 u_2 \rangle / U_\infty^2$  profiles on the suction side are shown in Figs. 30 (A) and (B). For better sense of virtual reality, the actual locations, denoted  $a - f$ , on the suction side of the SD7003 airfoil are used, as shown in Fig. 30 (A). Moreover, Fig. 30 (B) focuses on the effects of eigenvalue perturbations ( $1c$ ,  $2c$ ,  $3c$ ) for each location. In Figs. 30 (A) and (B), uncertainty bounds are depicted by gray regions. Figure 30 (A) clearly shows an enveloping behavior with respect to the baseline prediction at each location. An increase in the size of uncertainty bounds is observed as the flow moves from  $a$  to  $b$ , reaching a maximum at  $c$ , which is consistent with the behavior shown in Fig. 27. This indicates that the most model form uncertainty is found in the region downstream of the LSB near  $X_R$ . While the generated uncertainty bounds are not sufficient to encompass the reference data in the aft portion of the LSB, the reason is partly due to the fact that the eigenspace perturbation method is unable to account for the limitations of rotation and curvature effects, as stated in the previous section. In addition, the excluded amplitude perturbation and eigenvector perturbation of the Reynolds stress tensor and the parametric uncertainty introduced in model coefficients might also lead to the insufficiency in the generated uncertainty bounds. Further downstream from  $X_R$ , the size of the uncertainty bounds

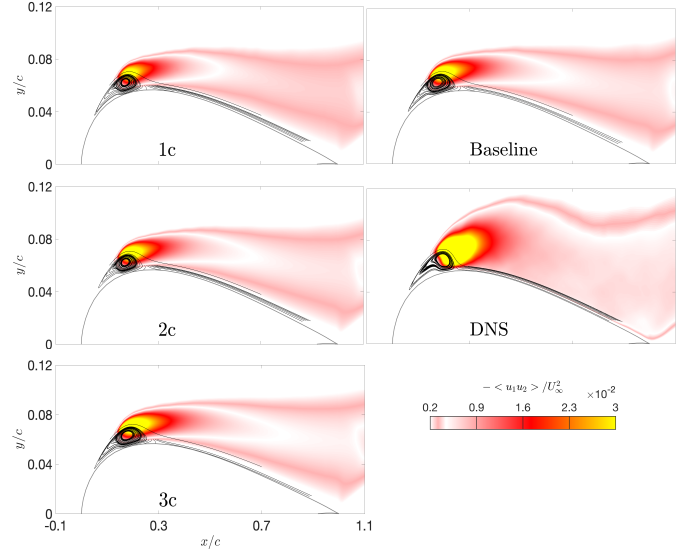


FIG. 29. Contours of  $-\langle u_1 u_2 \rangle / U_\infty^2$  for  $1c$ ,  $2c$  and  $3c$  perturbations at  $Tu = 0.03\%$ . Baseline prediction is provided for reference, and in-house DNS data<sup>32</sup> are included for comparison. Streamlines show the size of the LSB on the suction side of the airfoil.

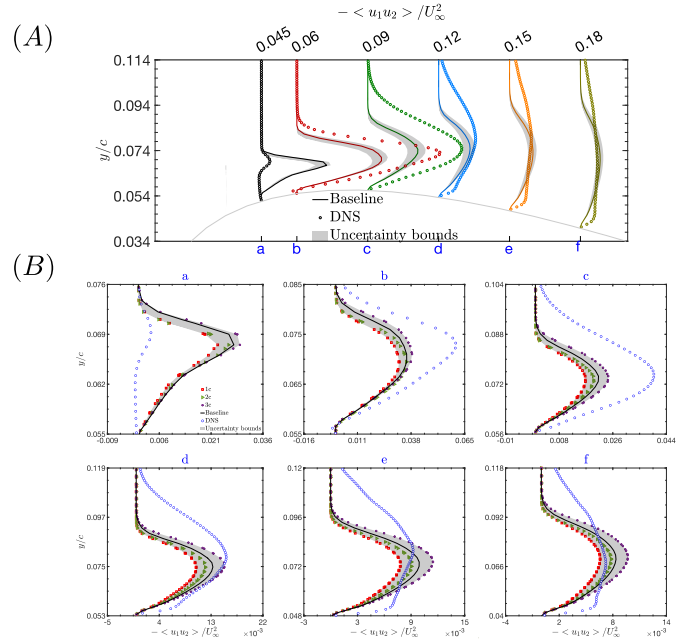


FIG. 30. (A) Profile of normalized Reynolds shear stress along the suction side of the SD7003 airfoil (geometry depicted by gray line): from left to right are  $a, b, c, d, e, f$  for  $x/c = 0.15, 0.2, 0.3, 0.4, 0.5$  and  $0.6$ , respectively. Displayed are uncertainty bounds for eigenvalue perturbations with uniform value of  $\Delta_B = 1$  at  $Tu = 0.03\%$ . Profile of baseline prediction is provided for reference. (B) Enlarged version of (A) at each location. Profiles of baseline prediction and  $1c$ ,  $2c$ , and  $3c$  perturbations are provided for reference.  $\circ$  in-house DNS data<sup>32</sup>.

gradually reduces, which shows a tendency of encompassing the in-house DNS data, reflecting increased trustworthiness within the attached TBL.

Figure 30 (B) scrutinizes closely the effects of the 1c, 2c and 3c perturbations at each location. From *a-f*, it is clear that the 1c and 2c perturbations under-predict the baseline prediction, while the 3c perturbation does the opposite. This confirms well with the behavior observed in the prediction for  $P_k$ , as shown in Fig. 21. This implies that Reynolds shear stress plays a key role in contributing to the turbulent production. At *a* (in the aft portion of the LSB), the 1c uncertainty bound shows a tendency to approach closer to the in-house DNS data, although a noticeable discrepancy is observed. At *b* (in the aft portion of the LSB) and *c* (downstream of the LSB near  $X_R$ ), the 3c perturbation increases the uncertainty bound toward the in-house DNS data, while both the 1c and 2c perturbations increase the uncertainty bounds in an opposite manner, namely, deviating from the in-house DNS data. As the flow proceeds further downstream within the attached turbulent boundary layer, the uncertainty bounds generated from the 1c, 2c and 3c perturbations begin to encompass the in-house DNS data, although discrepancies in the near-wall region as well as in the outer region of the flow are observed. Overall, the model form uncertainty is relatively small within the attached turbulent boundary layer, which indicates more trustworthy results than that for the LSB.

## V. CONCLUSIONS

The goal of this study was to advance our understanding of a physics-based approach to quantify model form uncertainty in transition RANS simulations of incompressible flows over a flat plate (T3A transition with  $Tu = 3.3\%$  and  $U_\infty = 5.4m/s$ ) and an airfoil (SD7003 airfoil with  $Re_c = 60,000$ ). Eigenvalue perturbations to the three extreme states (1c, 2c, and 3c) of the barycentric map has been investigated using the eigenspace perturbation framework by Emory *et al.*<sup>9</sup>, which has been implemented in a user-friendly fashion into the open-source OpenFOAM software. The eigenspace perturbation method directly injects perturbations to the Reynolds stress tensor, resulting in a perturbed velocity field by solving the momentum equations. The perturbations were conducted through a decomposition of the Reynolds stress tensor, i.e., perturbing eigenvalues of the anisotropy tensor.

### A. T3A

The SST  $k - \omega$  LM model successfully captured the laminar-turbulent transition over a flat plate, and showed overall good agreement between the prediction for the skin friction coefficient and the experimental data of<sup>48</sup>. On the other hand, the SST  $k - \omega$  and  $k - \varepsilon$  models clearly failed to capture the transition process, characterized by a trough in the prediction for the skin friction coefficient given by SST  $k - \omega$  LM. Most model form uncertainty was concentrated at the trough, in which eigenvalue perturbations exhibited an opposite way

compared to that for the turbulent region downstream of the trough. The size of uncertainty bound tended to increase linearly with the magnitude of  $\Delta_B$  for all three models. An important conclusion was drawn: the degree of response to the eigenvalue perturbations depends on which turbulence model is being used and which QoIs are being observed. From the contours of  $k/U_\infty^2$ , a bump at the leading edge of the flat plate marks laminar-turbulent transition, which corresponds to the location of the trough in skin friction coefficient plot.

### B. SD7003 airfoil

The predictions for the important transition parameters ( $X_S$ ,  $X_T$ , and  $X_R$ ) for  $Tu = 0.03\%$  were overall in good agreement with the reference data of<sup>32,54,55</sup> than that for  $Tu = 0.5\%$ . Overall, the predictions for the skin friction coefficient for  $Tu = 0.03\%$  in the fore portion of the LSB better matched the reference data than that for  $Tu = 0.5\%$ , while a relatively large discrepancy was found in the aft portion. This is consistent with the predictions by<sup>8,51,61</sup>. When the eigenvalue perturbations to the mean velocity profile and the Reynolds shear stress profile were plotted in the aft portion, an enveloping behavior was observed. It was interesting to note that a series of linear increments in  $\Delta_B$  led to linear responses in the increasing size of uncertainty bound for both the mean velocity profile and the Reynolds shear stress profile.

The anisotropy states of the Reynolds stress tensor were also analyzed using the Lumley's invariant map and the barycentric map. The Boussinesq anisotropy states based on the SST  $k - \omega$  LM model were clustered around the plane strain line due to the two-dimensional flow condition. On the other hand, the anisotropy states for in-house DNS in the aft portion of the LSB showed an oblate spheroid at the wall, and gradually transitioned to a prolate spheroid with increasing distance from the wall. This revealed that the laminar-turbulent transition tended to damp the streamwise stresses in the near-wall region. Downstream of  $X_R$  in the turbulent boundary layer, anisotropy states shifted from the axisymmetric contraction state to the two-component state. Away from the wall anisotropy states gradually shifted toward the axisymmetric expansion state, indicating increasing streamwise stresses.

The contours of the instantaneous velocity field on the suction side of the SD7003 airfoil were plotted at four different times, i.e.,  $T_0 - T_3$ . The LSB structure first originated at  $T_0$ , and vortex pairing began at  $T_1$ , then coalesced vortices to become a single and larger vortex at  $T_2$ , followed by vortex shedding breaking down to smaller stochastic small-scale structures at  $T_3$  when the LSB moved nearer to the leading edge. The 1c perturbation showed a tendency to suppress the evolution of the LSB, while the 3c perturbation fostered the formation of it instead.

Turbulent production  $P_k$  over the SD7003 airfoil peaked in the LSB, and 1c perturbation gave a lower production compared to the baseline prediction, while the opposite was true for the 3c perturbation. Besides, the 2c perturbation gave comparable magnitude of  $P_k$  to the baseline prediction.

When the uncertainty bounds for  $C_f$  over the airfoil for  $Tu = 0.03\%$  and  $Tu = 0.5\%$  were plotted, the  $1c$  and  $2c$  perturbations yielded a smaller magnitude of  $C_f$  (enhancing  $\langle U \rangle$ ) (larger negative value of  $C_f$ ) than the  $3c$  perturbation (reducing  $\langle U \rangle$ ) in the trough (aft portion of the LSB). This behavior is qualitatively similar to the UQ analysis for  $C_f$  for a turbulent flow over a backward-facing step<sup>13</sup>. In addition, the  $1c$  and  $2c$  perturbations shifted the  $X_R$  in the upstream direction, suppressing the LSB length, which showed a tendency to approach closer to the reference data for  $Tu = 0.03\%$ . While, the  $3c$  perturbation did the opposite. This behavior has been observed by other researchers as well, e.g.,<sup>11–13</sup>. In general, the SST  $k - \omega$  LM model was less sensitive to the eigenvalue perturbations for  $Tu = 0.5\%$  than  $Tu = 0.03\%$ .  $X_R$  for  $Tu = 0.03\%$  was well captured within the uncertainty bounds.

The uncertainty bounds for  $C_p$  over the airfoil for  $Tu = 0.03\%$  and  $Tu = 0.5\%$  were also analyzed. The model form uncertainty was most prevalent at the flat spot (fore portion of the LSB) as well as in the region around  $X_R$  (aft portion of the LSB), with the  $1c$  and  $2c$  perturbations giving a larger value of  $C_p$  than the baseline prediction, while the  $3c$  perturbation did the opposite, hence an enveloping behavior was observed. On the other hand, no discernible uncertainty bounds were observed for the rest regions, indicating a low level of the model form uncertainty. Overall, the size of the uncertainty bounds for  $Tu = 0.03\%$  was larger than that for  $Tu = 0.5\%$ .

The contours of the dimensionless mean velocity  $\langle U \rangle / U_\infty$  over the airfoil for  $Tu = 0.03\%$  were plotted in an  $xy$  plane, a large recirculating region was found in the region of reverse flow ( $\langle U \rangle / U_\infty < 0$ ). The size of reverse flow became smaller under the  $1c$  and  $2c$  perturbations, while the  $3c$  perturbation bolstered the region of reverse flow. The dimensionless mean velocity  $\langle U \rangle / U_\infty$  profiles across the suction side of the airfoil were also plotted in shifted coordinates  $y/c|_o$ , the lower sections of the  $\langle U \rangle / U_\infty$  profile in the aft portion of the LSB showed relatively good agreement with the in-house DNS data<sup>32</sup>. The size of uncertainty bounds was negligible at  $X_T$ , then reached its maximum near  $X_R$ . Downstream of  $X_R$ ,  $\langle U \rangle / U_\infty$  increased in magnitude under the  $1c$  and  $2c$  perturbations compared to the baseline prediction, while the  $3c$  perturbation did the opposite. This behavior is qualitatively similar to that observed by Luis *et al.*<sup>14</sup>.

The contours of the dimensionless Reynolds shear stress  $-\langle u_1 u_2 \rangle / U_\infty^2$  over the airfoil for  $Tu = 0.03\%$  were plotted in an  $xy$  plane, a peak appeared around the LSB. The  $1c$  perturbation under-predicted the baseline prediction, while the  $3c$  perturbation increased the magnitude of  $-\langle u_1 u_2 \rangle / U_\infty^2$ , showing a tendency to approach closer to the in-house DNS data. The predicted  $-\langle u_1 u_2 \rangle / U_\infty^2$  profiles were also plotted based on the actual locations on the suction side of the airfoil, and an enveloping behavior with respect to the baseline prediction was observed. The size of uncertainty bounds increased to its maximum near  $X_R$ , followed by a smooth reduction as the flow proceeded downstream of  $X_R$ . Overall, the  $1c$  and  $2c$  perturbations under-predicted the baseline prediction, while the  $3c$  perturbation did the opposite. Downstream of  $X_R$  in the attached turbulent boundary layer, uncertainty bounds generated from the  $1c$ ,  $2c$ , and  $3c$  perturbations began to encompass

near-wall sections of the in-house DNS profiles.

Overall, the eigenspace perturbation framework was effective in constructing uncertainty bounds for a variety of QoIs. Future work will focus on perturbation to the amplitude of Reynolds stress and the eigenvectors of the Reynolds stresses to complete the full range of the model form uncertainty in the SST  $k - \omega$  LM model. Also a wider range of RANS-based transition models will be tested using the eigenspace perturbation framework.

## ACKNOWLEDGMENTS

The support of the Natural Sciences and Engineering Research Council (NSERC) of Canada for the research program of Professor Xiaohua Wu and Professor David E. Rival is gratefully acknowledged. The author Dr. Minghan Chu thanks Dr. Aashwin Ananda Mishra for providing valuable feedback and helpful discussions.

## DATA AVAILABILITY STATEMENT

The data that support the findings of this study are available from the corresponding author upon reasonable request.

## REFERENCES

- <sup>1</sup>R. Pecnik and W. Sanz, "Application of the turbulent potential model to heat transfer predictions on a turbine guide vane," (2007).
- <sup>2</sup>F. Menter, T. Esch, and S. Kubacki, "Transition modelling based on local variables," in *Engineering Turbulence Modelling and Experiments 5* (Elsevier, 2002) pp. 555–564.
- <sup>3</sup>F. Menter, R. Langtry, S. Likki, Y. Suzen, P. Huang, and S. Vo"lker, "A correlation-based transition model using local variables: Part i—model formulation," in *Turbo Expo: Power for Land, Sea, and Air*, Vol. 41693 (2004) pp. 57–67.
- <sup>4</sup>F. Menter, R. Langtry, and S. V"olker, "Transition modelling for general purpose cfd codes," *Flow, turbulence and combustion* **77**, 277–303 (2006).
- <sup>5</sup>R. B. Langtry and F. R. Menter, "Correlation-based transition modeling for unstructured parallelized computational fluid dynamics codes," *AIAA journal* **47**, 2894–2906 (2009).
- <sup>6</sup>F. R. Menter, P. E. Smirnov, T. Liu, and R. Avancha, "A one-equation local correlation-based transition model," *Flow, Turbulence and Combustion* **95**, 583–619 (2015).
- <sup>7</sup>L. Wei, X. Ge, J. George, and P. Durbin, "Modeling of laminar-turbulent transition in boundary layers and rough turbine blades," *Journal of Turbomachinery* **139** (2017).
- <sup>8</sup>N. Tousi, M. Coma, J. Bergadà, J. Pons-Prats, F. Mellibovsky, and G. Bugeada, "Active flow control optimisation on sd7003 airfoil at pre and post-stall angles of attack using synthetic jets," *Applied Mathematical Modelling* **98**, 435–464 (2021).
- <sup>9</sup>M. Emory, J. Larsson, and G. Iaccarino, "Modeling of structural uncertainties in reynolds-averaged navier-stokes closures," *Physics of Fluids* **25**, 110822 (2013).
- <sup>10</sup>M. Emory, V. Terrapon, R. Pecnik, and G. Iaccarino, "Characterizing the operability limits of the hyshot ii scramjet through rans simulations," in *17th AIAA international space planes and hypersonic systems and technologies conference* (2011) p. 2282.
- <sup>11</sup>C. Gorié, S. Zeoli, M. Emory, J. Larsson, and G. Iaccarino, "Epistemic uncertainty quantification for reynolds-averaged navier-stokes modeling of

- separated flows over streamlined surfaces,” *Physics of Fluids* **31**, 035101 (2019).
- <sup>12</sup>A. Mishra and G. Iaccarino, “Rans predictions for high-speed flows using enveloping models,” arXiv preprint arXiv:1704.01699 (2017).
- <sup>13</sup>G. Iaccarino, A. A. Mishra, and S. Ghili, “Eigenspace perturbations for uncertainty estimation of single-point turbulence closures,” *Physical Review Fluids* **2**, 024605 (2017).
- <sup>14</sup>L. F. Cremades Rey, D. F. Hinz, and M. Abkar, “Reynolds stress perturbation for epistemic uncertainty quantification of rans models implemented in openfoam,” *Fluids* **4**, 113 (2019).
- <sup>15</sup>N. Razaaly, G. Gori, G. Iaccarino, and P. M. Congedo, “Optimization of an orc supersonic nozzle under epistemic uncertainties due to turbulence models,” in *GPPS 2019-Global Power and Propulsion Society* (2019).
- <sup>16</sup>L. W. Cook, A. Mishra, J. Jarrett, K. Willcox, and G. Iaccarino, “Optimization under turbulence model uncertainty for aerospace design,” *Physics of Fluids* **31**, 105111 (2019).
- <sup>17</sup>A. A. Mishra, J. Mukhopadhaya, J. Alonso, and G. Iaccarino, “Design exploration and optimization under uncertainty,” *Physics of Fluids* **32**, 085106 (2020).
- <sup>18</sup>M. Matha and C. Morsbach, “Extending turbulence model uncertainty quantification using machine learning,” arXiv preprint arXiv:2202.01560 (2022).
- <sup>19</sup>M. Matha, K. Kucharczyk, and C. Morsbach, “Assessment of data-driven reynolds stress tensor perturbations for uncertainty quantification of rans turbulence models,” in *AIAA AVIATION 2022 Forum* (2022) p. 3767.
- <sup>20</sup>C. García-Sánchez, D. Philips, and C. Gorié, “Quantifying inflow uncertainties for cfd simulations of the flow in downtown oklahoma city,” *Building and environment* **78**, 118–129 (2014).
- <sup>21</sup>C. Gorié, C. Garcia-Sanchez, and G. Iaccarino, “Quantifying inflow and rans turbulence model form uncertainties for wind engineering flows,” *Journal of Wind Engineering and Industrial Aerodynamics* **144**, 202–212 (2015).
- <sup>22</sup>H. Xiao, J.-L. Wu, J.-X. Wang, R. Sun, and C. Roy, “Quantifying and reducing model-form uncertainties in reynolds-averaged navier–stokes simulations: A data-driven, physics-informed bayesian approach,” *Journal of Computational Physics* **324**, 115–136 (2016).
- <sup>23</sup>J.-L. Wu, J.-X. Wang, and H. Xiao, “A bayesian calibration–prediction method for reducing model-form uncertainties with application in rans simulations,” *Flow, Turbulence and Combustion* **97**, 761–786 (2016).
- <sup>24</sup>E. J. Parish and K. Duraisamy, “A paradigm for data-driven predictive modeling using field inversion and machine learning,” *Journal of Computational Physics* **305**, 758–774 (2016).
- <sup>25</sup>H. Xiao, J.-X. Wang, and R. G. Ghanem, “A random matrix approach for quantifying model-form uncertainties in turbulence modeling,” *Computer Methods in Applied Mechanics and Engineering* **313**, 941–965 (2017).
- <sup>26</sup>J.-X. Wang, J.-L. Wu, and H. Xiao, “Physics-informed machine learning approach for reconstructing reynolds stress modeling discrepancies based on dns data,” *Physical Review Fluids* **2**, 034603 (2017).
- <sup>27</sup>J.-X. Wang, J. Wu, J. Ling, G. Iaccarino, and H. Xiao, “A comprehensive physics-informed machine learning framework for predictive turbulence modeling,” arXiv preprint arXiv:1701.07102 (2017).
- <sup>28</sup>J. F. Heyse, A. A. Mishra, and G. Iaccarino, “Estimating rans model uncertainty using machine learning,” *Journal of the Global Power and Propulsion Society* **2021**, 1–14 (2021).
- <sup>29</sup>J. Mukhopadhaya, B. T. Whitehead, J. F. Quindlen, J. J. Alonso, and A. W. Cary, “Multi-fidelity modeling of probabilistic aerodynamic databases for use in aerospace engineering,” *International Journal for Uncertainty Quantification* **10** (2020).
- <sup>30</sup>N. Nigam, S. Mohseni, J. Valverde, S. Voronin, J. Mukhopadhaya, and J. J. Alonso, “A toolset for creation of multi-fidelity probabilistic aerodynamic databases,” in *AIAA Scitech 2021 Forum* (2021) p. 0466.
- <sup>31</sup>S. Banerjee, R. Krahl, F. Durst, and C. Zenger, “Presentation of anisotropy properties of turbulence, invariants versus eigenvalue approaches,” *Journal of Turbulence* , N32 (2007).
- <sup>32</sup>H. Zhang, *Turbulent and Non-Turbulent Interfaces in Low Mach Number Airfoil Flows*, Ph.D. thesis, Queen’s University (Canada) (2021).
- <sup>33</sup>J. L. Lumley, “Computational modeling of turbulent flows,” in *Advances in applied mechanics*, Vol. 18 (Elsevier, 1979) pp. 123–176.
- <sup>34</sup>S. B. Pope, “Turbulent flows,” (2001).
- <sup>35</sup>P. A. Durbin and B. P. Reif, *Statistical theory and modeling for turbulent flows* (John Wiley & Sons, 2011).
- <sup>36</sup>F. Menter, “Zonal two equation kw turbulence models for aerodynamic flows,” in *23rd fluid dynamics, plasmadynamics, and lasers conference* (1993) p. 2906.
- <sup>37</sup>A. Hellsten, “Some improvements in menter’s k-omega sst turbulence model,” in *29th AIAA, Fluid Dynamics Conference* (1998) p. 2554.
- <sup>38</sup>F. Menter and T. Esch, “Elements of industrial heat transfer predictions,” in *16th Brazilian Congress of Mechanical Engineering (COBEM)*, Vol. 109 (sn, 2001) pp. 117–127.
- <sup>39</sup>F. R. Menter, M. Kuntz, and R. Langtry, “Ten years of industrial experience with the sst turbulence model,” *Turbulence, heat and mass transfer* **4**, 625–632 (2003).
- <sup>40</sup>F. R. Menter, R. B. Langtry, S. Likki, Y. Suzen, P. Huang, and S. Völker, “A correlation-based transition model using local variables—part i: model formulation,” *Journal of turbomachinery* **128**, 413–422 (2006).
- <sup>41</sup>S. El Tahry, “K-epsilon equation for compressible reciprocating engine flows,” *Journal of Energy* **7**, 345–353 (1983).
- <sup>42</sup>B. E. Launder and D. B. Spalding, “The numerical computation of turbulent flows,” in *Numerical prediction of flow, heat transfer, turbulence and combustion* (Elsevier, 1983) pp. 96–116.
- <sup>43</sup>M. Emory, R. Pecnik, and G. Iaccarino, “Modeling structural uncertainties in reynolds-averaged computations of shock/boundary layer interactions,” in *49th AIAA Aerospace Sciences Meeting including the New Horizons Forum and Aerospace Exposition* (2011) p. 479.
- <sup>44</sup>C. Gorié, M. Emory, J. Larsson, and G. Iaccarino, “Epistemic uncertainty quantification for rans modeling of the flow over a wavy wall,” *Center for turbulence research, annual research briefs* , 81–91 (2012).
- <sup>45</sup>A. Mishra and G. Iaccarino, “Theoretical analysis of tensor perturbations for uncertainty quantification of reynolds averaged and subgrid scale closures,” *Physics of Fluids* **31**, 075101 (2019).
- <sup>46</sup>A. E. Winkelman and J. B. Barlow, “Flowfield model for a rectangular planform wing beyond stall,” *AIAA Journal* **18**, 1006–1008 (1980).
- <sup>47</sup>S. D. Hornshøj-Møller, P. D. Nielsen, P. Foroughi, and M. Abkar, “Quantifying structural uncertainties in reynolds-averaged navier–stokes simulations of wind turbine wakes,” *Renewable Energy* **164**, 1550–1558 (2021).
- <sup>48</sup>P. Roach, “The influence of a turbulent free-stream on zero pressure gradient transitional boundary layer development: Part 1. test cases t3a and t3b,” in *ERCOFTAC Workshop, Lausanne, 1990* (1990).
- <sup>49</sup>H. G. Weller, G. Tabor, H. Jasak, and C. Fureby, “A tensorial approach to computational continuum mechanics using object-oriented techniques,” *Computers in physics* **12**, 620–631 (1998).
- <sup>50</sup>J. P. Van Doormaal and G. D. Raithby, “Enhancements of the simple method for predicting incompressible fluid flows,” *Numerical heat transfer* **7**, 147–163 (1984).
- <sup>51</sup>P. Catalano and R. Tognaccini, “Rans analysis of the low-reynolds number flow around the sd7003 airfoil,” *Aerospace Science and Technology* **15**, 615–626 (2011).
- <sup>52</sup>J. H. Ferziger, M. Perić, and R. L. Street, *Computational methods for fluid dynamics*, Vol. 3 (Springer, 2002).
- <sup>53</sup>J. J. Alonso, M. S. Eldred, P. Constantine, K. Duraisamy, C. Farhat, G. Iaccarino, and J. Jakeman, “Scalable environment for quantification of uncertainty and optimization in industrial applications (sequoia),” in *19th AIAA Non-Deterministic Approaches Conference* (2017) p. 1327.
- <sup>54</sup>M. Galbraith and M. Visbal, “Implicit large eddy simulation of low-reynolds-number transitional flow past the sd7003 airfoil,” in *40th fluid dynamics conference and exhibit* (2010) p. 4737.
- <sup>55</sup>D. J. Garmann, M. R. Visbal, and P. D. Orkwis, “Comparative study of implicit and subgrid-scale model large-eddy simulation techniques for low-reynolds number airfoil applications,” *International Journal for Numerical Methods in Fluids* **71**, 1546–1565 (2013).
- <sup>56</sup>M. Gaster, *The structure and behaviour of laminar separation bubbles* (Citeseer, 1967).
- <sup>57</sup>I. Tani, “Low-speed flows involving bubble separations,” *Progress in Aerospace Sciences* **5**, 70–103 (1964).
- <sup>58</sup>M. O’meara and T. J. Mueller, “Laminar separation bubble characteristics on an airfoil at low reynolds numbers,” *AIAA journal* **25**, 1033–1041 (1987).
- <sup>59</sup>M. S. Boutilier and S. Yarusevych, “Parametric study of separation and transition characteristics over an airfoil at low reynolds numbers,” *Experi-*

- ments in fluids **52**, 1491–1506 (2012).
- <sup>60</sup>C. De Santis, P. Catalano, and R. Tognaccini, “Model for enhancing turbulent production in laminar separation bubbles,” *AIAA Journal*, 1–15 (2021).
- <sup>61</sup>L. F. Bernardos, F. Richez, and V. Gleize, “Rans modeling of laminar separation bubbles around airfoils at low reynolds conditions,” in *AIAA Aviation 2019 Forum* (2019) p. 2922.
- <sup>62</sup>M. S. Istvan, J. W. Kurelek, and S. Yarusevych, “Turbulence intensity effects on laminar separation bubbles formed over an airfoil,” *AIAA Journal* **56**, 1335–1347 (2018).
- <sup>63</sup>D. Lengani, D. Simoni, M. Ubaldi, and P. Zunino, “Pod analysis of the unsteady behavior of a laminar separation bubble,” *Experimental thermal and fluid science* **58**, 70–79 (2014).
- <sup>64</sup>M. Emory and G. Iaccarino, “Visualizing turbulence anisotropy in the spatial domain with componentality contours,” *Center for Turbulence Research Annual Research Briefs*, 123–138 (2014).
- <sup>65</sup>W. N. Edeling, G. Iaccarino, and P. Cinnella, “Data-free and data-driven rans predictions with quantified uncertainty,” *Flow, Turbulence and Combustion* **100**, 593–616 (2018).
- <sup>66</sup>J. H. Wamuff, “Evolution of a wave packet into vortex loops in a laminar separation bubble,” *Journal of Fluid Mechanics* **397**, 119–169 (1999).
- <sup>67</sup>O. Marxen, M. Lang, U. Rist, and S. Wagner, “A combined experimental/numerical study of unsteady phenomena in a laminar separation bubble,” *Flow, Turbulence and Combustion* **71**, 133–146 (2003).
- <sup>68</sup>B. McAuliffe and M. Yaras, “Transition mechanisms in separation bubbles under low and elevated freestream turbulence,” in *Turbo Expo: Power for Land, Sea, and Air*, Vol. 47934 (2007) pp. 1063–1076.
- <sup>69</sup>M. Alam and N. D. Sandham, “Direct numerical simulation of ‘short’ laminar separation bubbles with turbulent reattachment,” *Journal of Fluid Mechanics* **410**, 1–28 (2000).
- <sup>70</sup>J. Wissink and W. Rodi, “Dns of a laminar separation bubble in the presence of oscillating external flow,” *Flow, turbulence and combustion* **71**, 311–331 (2003).
- <sup>71</sup>D. Simoni, M. Ubaldi, P. Zunino, and F. Bertini, “Transition mechanisms in laminar separation bubbles with and without incoming wakes and synthetic jet effects,” *Experiments in fluids* **53**, 173–186 (2012).
- <sup>72</sup>J. W. Kurelek, A. R. Lambert, and S. Yarusevych, “Coherent structures in the transition process of a laminar separation bubble,” *AIAA Journal* **54**, 2295–2309 (2016).
- <sup>73</sup>J. M. Lin and L. L. Pauley, “Low-reynolds-number separation on an airfoil,” *AIAA journal* **34**, 1570–1577 (1996).
- <sup>74</sup>M. Kiya and K. Sasaki, “Structure of large-scale vortices and unsteady reverse flow in the reattaching zone of a turbulent separation bubble,” *Journal of Fluid Mechanics* **154**, 463–491 (1985).
- <sup>75</sup>K. Zhang and D. E. Rival, “Direct lagrangian method to characterize entrainment dynamics using particle residence time: a case study on a laminar separation bubble,” *Experiments in Fluids* **61**, 1–11 (2020).